Argonne NATIONAL LABORATORY

ANL/LWRS-22/1

Hybrid Artificial Intelligence-Machine Learning and Finite Element-based Digital Twin Predictive Modeling Framework for PWR Coolant System Components: Updates on Multi-Time-Series-3D-Location Dependent Usage Factor Prediction

LWRS milestone Report Number: M3LW-22OR0402043

Nuclear Science and Engineering Division

ANL/LWRS-22/1

Hybrid Artificial Intelligence-Machine Learning and Finite Element-based Digital Twin Predictive Modeling Framework for PWR Coolant System Components: Updates on Multi-Time-Series-3D-Location Dependent Usage Factor Prediction

LWRS milestone Report Number: M3LW-22OR0402043

Prepared by
Subhasish Mohanty
Nuclear Science and Engineering Division, Argonne National Laboratory

Prepared for
DOE Light Water Reactor Sustainability (LWRS) Program

June 30, 2022

This page intentionally left blank

ABSTRACT

The long-term operation (LTO) of nuclear power plants (NPP) beyond their original design life of 40 years can lead to more material damage associated with cyclic fatigue under thermal-mechanical loading cycles and associated long-term exposure of reactor material to the deleterious reactor-coolant environments. However, under this LTO condition, the reactor components can still safely operate but may require more frequent Nondestructive Evaluation (NDE) of reactor components. Requiring frequent NDE inspections may lead to frequent NPP shutdowns which can lead to power outages and additional NDE inspection cost-related economic loss. The economic loss can be minimized by reducing uncertainty in life estimation of safety-critical pressure boundary components and by implementing a more digital approach such as using upcoming digital-twin (DT) technology for predicting the structural states (e.g., time and location dependent inside/outside thickness temperature, stress, strain, plastic deformation, etc.) and associated fatigue life of a component in real time. The DT framework is based on limited experimental data, Artificial-Intelligence (AI)-Machine-Learning (ML) and multiphysics-computational-mechanics such as finite element- (FE) based models. Given the real-time thermal-hydraulic process measurements from several existing plant sensors, the overall goal of the DT framework is to predict the cumulative usage factors or equivalent fatigue lives in real time and at any random 3D location of the components. This includes inaccessible locations such as inside the thickness location of a component. This prediction can be at thousands to millions of 3D point clouds or locations such as conventional FE-based models, but without running an FE model in real time. Towards this goal, some of the major contributions made during FY22 follow:

a. Based on earlier developed system-level FE model of a reactor coolant system (RCS) and associated stress analysis results, we estimated the fatigue lives of different components. Based on these results, we determined that the hot-leg side nozzle of surge line can be an issue, particularly for long-term operation of nuclear reactors. The simulated component-level strain profile (under realistic multi-axial multi-physics connected system boundary conditions) can guide the selection of appropriate test inputs for conducting laboratory-scale environmental-assisted-fatigue (EAF) tests for further evaluating the fatigue life of a component, which is an objective of future work. These results are geometry-specific and qualitative. But since most of NPPs have very similar configurations, we can expect similar qualitative results. Nevertheless, the reported results are representative and can be used as a guideline to focus NDE-related inspections for a specific region rather than the entire RCS. Additionally, the resulting FE-simulated structural states can be used as virtual sensor data for training the AI-ML based data-driven models of the overall DT framework.

b. A preliminary MySQL-based database architected, which is the backbone storage system of the proposed DT framework for storing both the real sensor data and 3D virtual sensor data (obtained through the above-mentioned system-level FE models). Additionally, we developed a python-based application programming interface (API) to interact with the database and other physics submodules or applications of the overall DT framework.

c. A software framework was developed to predict time and 3D-location-dependent cumulative usage factors, or the equivalent fatigue lives given the associated time- and location-dependent mechanical strain profiles. The algorithm or the associated software stacks will eventually be linked to the overall DT framework.

TABLE OF CONTENTS

LIST OF FIGURES

LIST OF TABLES

ABBREVIATIONS

AI-ML: Artificial Intelligence-Machine Learning
API: Application Programming Interface
CAD: Computer Aided Design
CFD: Computational Fluid Dynamics
CL: Cold Leg
CUF: Cumulative Usage Factor
CUF_{en}: Cumulative Usage Factor under PWR Coolant Water Environment
DL: Deep-Learning
DMW: Dissimilar Metal Weld
DT: Digital Twin
EAF: Environmental Assisted Fatigue
FE: Finite Element
HL: Hot Leg
ID: Inner Diameter
LAS: Low Alloy Steel
LTO: Long Term Operation
NDE: Nondestructive Evaluation
NPP: Nuclear Power Plant
OD: Outer Diameter
PRZ: Pressurizer
PWR: Pressurized Water Reactor
RCS: Reactor Coolant System
RPV: Reactor Pressure Vessel
SG: Steam Generator
SL: Surge Line
SMW: Similar Metal Weld
SS: Stainless Steel

ACKNOWLEDGMENTS

This research was supported through the U.S. Department of Energy's Light Water Reactor Sustainability Program Materials Research Pathway under the work package of environmentally assisted fatigue study with the pathway lead Dr. Thomas. M. Rosseel and deputy pathway lead Dr. Xiang (Frank) Chen.

1 Introduction

Due to climate change and economical requirements, the U.S. operating nuclear fleet needs to operate well beyond the original design life of 40 years [1]. While the LTO of NPPs well beyond their design life may be safe, extensive study is required, particularly when the life of the reactor extends to 80 years or beyond. For example, NPP operation under LTO can lead to more material damage associated with cyclic fatigue under thermal-mechanical loading cycles and associated long-term exposure of reactor material to the deleterious reactor-coolant environments. There are concerns about the multi-metal nozzles and high-stress base-metal components. These components can have high plastic deformation and resulting residual stress-strain that may adversely affect the integrity of safety-critical NPP components under LTOs. The structural integrity can be further affected if the component is exposed to corrosive reactor-coolant environments. For example, the life of a reactor component can be significantly shortened under the reactor coolant environment compared to air conditions [2,3]. Particularly, when a component with high strain interacts with a corrosive reactor coolant environment, the life of that component may be significantly shortened depending on the type of material, strain amplitude, strain rates, residual strain, temperature of operations, and the coolant water chemistry.

As reactors operate much longer than the original design life, more cracking of components is expected due to the long-term exposure of reactor material to the deleterious reactor-coolant environment. For that reason, accurate life prediction of reactor components is necessary for the overall safety of NPPs. Accurate prediction of structural integrity of a reactor component is challenging because of complex intermixing of multiple failure modes/causes, such as (1) residual strain associated with the manufacturing process and loading cycle, (2) the evolution of reactor material properties associated with cyclic loading and reactor-coolant environment, and (3) multiaxial stress-strain states associated with system-level connected-system-thermal-mechanical-boundary conditions. The individual effects of these failure modes and their interaction to each other need to be characterized and modeled combinedly. Along with mechanisticl understanding and predicting the failure modes and its progression, it is also essential for predicting the associated component states economically. Note that currently the NPP operator must depend on NDE-based-periodic inspections of plant components. However, when plants operate much longer than the original design life, more cracking of components is expected, requiring more frequent NDE inspections and resulting costs. The NDE and related operational cost can be reduced through online monitoring and by using upcoming technology such as DT. The DT framework must be based on system-level physics-based modeling such as through 3D FE models and their data-driven representations, including those based on AI-ML techniques. In our earlier LWRS-supported works [4,5], we developed some of the AI-ML- and DT- related predictive techniques. However, the overall DT framework is in a very nascent stage and needs to be further developed. Towards that goal, our FY22 work focused on further developing the DT framework and the related real-time predictive modeling techniques.

In **Section-2** we present life prediction results of the some of the RCS components subjected to realistic multiaxial and connected-system thermal-mechanical boundary conditions.

In **Section-3** we present preliminary works related to a MySQL database that will form the backbone storage system of the proposed DT framework. In this section, we also present preliminary work related to the development of an application programming interface (API) that will eventually link the database and various predictive models or applications.

In **Section-4** we present preliminary work and results related to the development of algorithms and related software for predicting time- and spatial-location dependent usage factors given a time- and spatial location-dependent mechanical strain profile.

2 Fatigue Life Estimation of PWR RCS Components under Connected-system thermal-mechanical Boundary Conditions

System-level thermal-mechanical-boundary conditions can significantly affect the multi-axial stress-strain states of a component. Under system-level loading, a reactor component can experience localized plastic zones and associated residual stress-strain (for example at the end of a reactor loading cycle). Unless a system-level analysis is performed that considers system-level connected system thermal-mechanical boundary conditions, we cannot assess the true picture of the component level strain and the associated fatigue lives. Based on our earlier presented system-level FE model of RCS components of a pressurized water reactor (PWR) [5], we developed a fatigue life estimation strategy. For completeness and easier reference to the physics and geometry involved, we briefly discuss the related FE model in this section. The details of the FE model are discussed in our earlier publication [5]. We also present the results related to fatigue lives of some RCS components.

2.1 Finite Element Model for Thermal-Mechanical Stress Analysis

Unlike a traditional single-component-based model, we used a system-level model for more accurately imposing the system-level thermal-mechanical boundary conditions associated with system-level thermal gradients and displacements (or strains). In the proposed system-level model, we considered the primary-loop RCS of a representative PWR as an example case. The major components of a PWR are Reactor Pressure Vessel (RPV), Steam Generator (SG), Hot Leg (HL), Cold Leg (CL), Surge Line (SL), and Pressurizer (PRZ). With a primary aim of estimating fatigue lives of HL and SL (as example components), we only modeled components such as RPV, SG and PRZ that are directly connected to HL and SL in the proposed system-level model. Since the HL and SL are at a (certain) height from the bottom of the RPV, we considered the entire RPV geometry. Whereas for SG and PRZ, we only modeled the bottom head of SG and PRZ since the HL or SL is connected at the bottom head of SG or PRZ.

Figure 2.1 shows the assembly-level ABAQUS model of the RPV, including the bottom heads of SG, PRZ, HL, SL, and their DMW nozzles. The bottom heads of RPV, SG, and PRZ were applied with fixed displacement boundary conditions, assuming they are skirt-supported with the top part of the skirt welded to the bottom head of the RPV, SG or PRZ and the bottom part of the skirt bolted to the ground pedestal. However, the actual reactor boundary conditions can vary from plant to plant. Nevertheless, our aim was to develop a methodology for system-level stress analysis to estimate the strain profiles and associated fatigue lives. The model was developed by using commercially available ABAQUS FE software. Individual nozzles of the HL and SL were modeled in detail with both dissimilar metal weld (DMW) and similar metal weld (SMW). The RPV, PRZ, and SG were modeled using low-allow steel (LAS) material properties, whereas the HL and SL were modeled using stainless-steel (SS) material properties. The RPV, SG, PRZ, HL, and SL were connected through DMW and SMW joints.

Figure 2.2 shows the CAD model and different materials of HL and its nozzles while Figure 2.3 shows the CAD model and different materials of SL and its nozzles. The individual components were meshed using 3D-hexahedral elements. For the high-level FE model discussed, this research did not conduct a specific mesh sensitivity analysis, although it is planned for future work. To reduce computational burden (with limited availability of ABAQUS licenses), the total number of elements of the overall assembly

model was limited to 60,000, but with finer mesh at nozzle areas. The DC3D8 and C3D8 linear 8-noded brick elements were used for the heat transfer and the subsequent stress analysis models, respectively.

Figure 2.4 shows the applied temperature transients at the ID surfaces of HL, CL (or RPV), and PRZ. The maximum temperature of RPV, HL, and PRZ is 287.78^{o}C, 326.4^{o}C, and 347.3^{o}C, respectively. Linearly scaled temperature boundary conditions were applied to the different sections of SL to simulate a transient thermal stratification condition. It is assumed that along the length of SL, the lowest temperature will be at the HL-end of SL (matching with the temperature of HL with a maximum temperature of 326.4^{o}C), whereas the highest temperature will be at the PRZ-end of SL (matching with the temperature of PRZ with maximum temperature of 347.3^{o}C). In Figure 2.4, the temperature boundary conditions are not directly measured, but rather are based on assumed conditions. These temperature profiles were created assuming a design-basis boundary condition, or the maximum anticipated ID temperatures that a typical PWR would experience at a given time. Further details can be found in our earlier work [5, 6]. We uniformly applied these temperature boundary conditions to the ID surfaces of the individual components, except for the surge line. To simulate a thermally stratified flow in SL [7], we applied different temperature boundary conditions to the different sections of SL. As mentioned above, the ID surfaces of the SL were divided into seven different sections and applied with seven assumed temperature transients. These transients were linearly interpolated between HL and PRZ temperatures in seven increasing increments, from HL to PRZ to the end of SL. Note that for more accurate temperature boundary conditions, the CFD analysis must be performed (as in [7]).

Figure 2.5 shows the applied pressure transients at the ID surfaces of all the primary-loop components (i.e., of RPV, HL, SL, PRZ) and bottom head of SG. Note that the stress analysis results reported in this paper are related to a typical design-basis loading cycle (shown in Figures 2.4 and 2.5). However, as mentioned before, resulting strain amplitude, stress amplitude, and residual strain can vary substantially from plant to plant depending on the thermal-mechanical boundary conditions. The system-level model described in this section is an example intended to demonstrate the need for a system-level model (with connected component thermal-mechanical boundary conditions) for more accurately estimating strain profile instead of a model based on a single component (with isolated thermal-mechanical boundary conditions).

The stress analysis model was developed using temperature-dependent mechanical properties, such as expansion coefficients, elastic modulus, yield stress, and kinematic hardening properties. Tables 2.1 through 2.5 show the summary of related mechanical properties used for the stress analysis model. Note that all the yield and hardening parameters are based on 0.05% offset-strain rather than the conventional 0.2% offset-strain yield limit. This better captures the plasticity region of a component [8]. Figure 2.6 shows the comparison of expansion coefficients for different materials used in the model. Note that all material properties and the expansion coefficients used in the FE models are directly based on our earlier tensile tests [8], which improve accuracy in the FE model for future experimental validation. We assume the manufacturing related residual stresses were incorporated in the FE model by using the material properties directly estimated based on the tensile test data of associated weld metals.

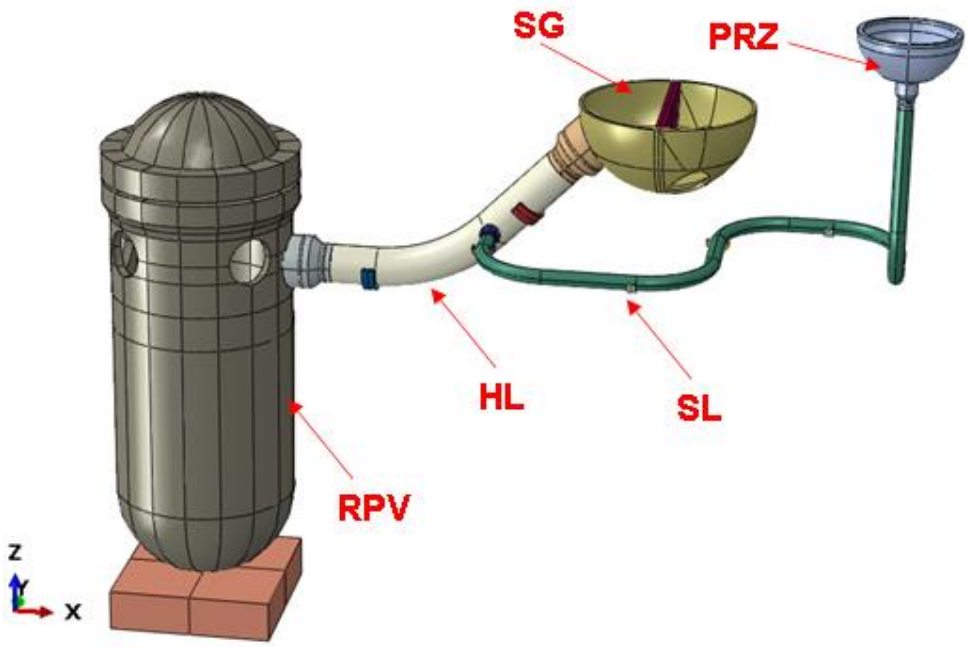

Figure 2. 1. Assembly-level ABAQUS-FE model of RPV.

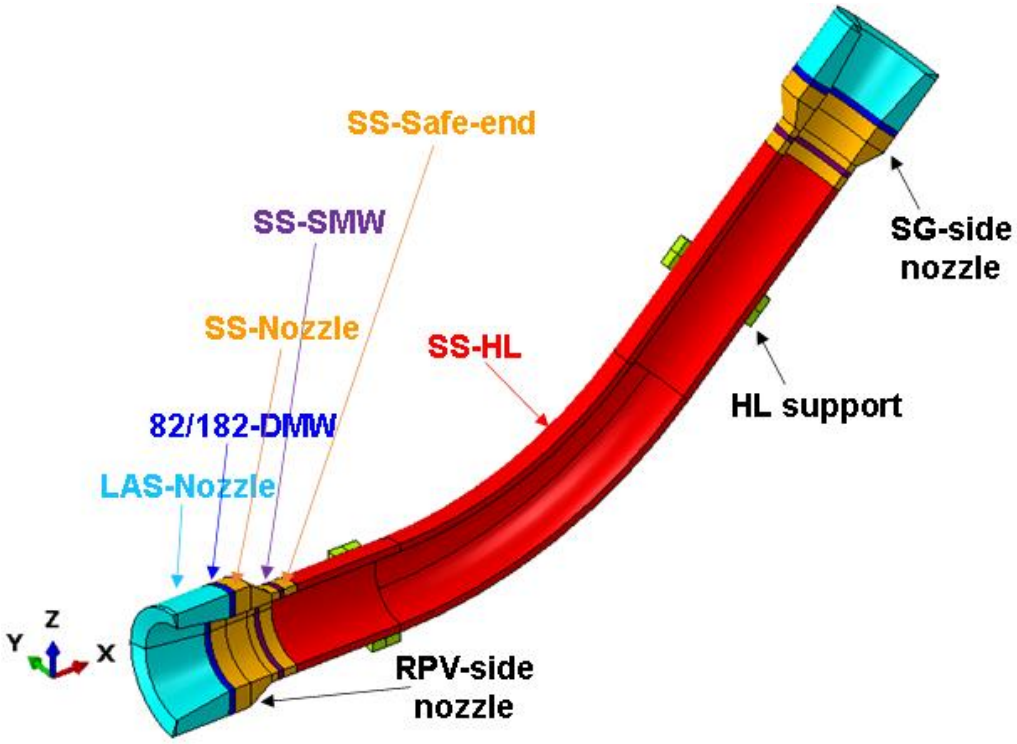

Figure 2. 2. ABAQUS-FE model and different materials of HL and its nozzles.

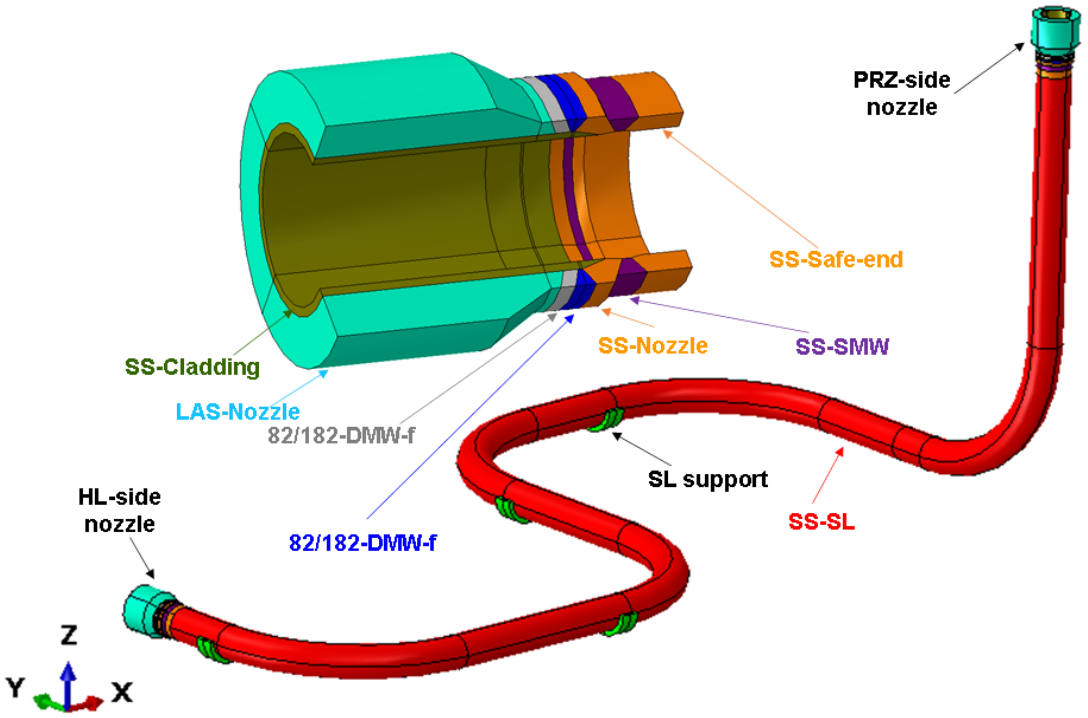

Figure 2. 3. ABAQUS-FE model and different materials of SL and its nozzles.

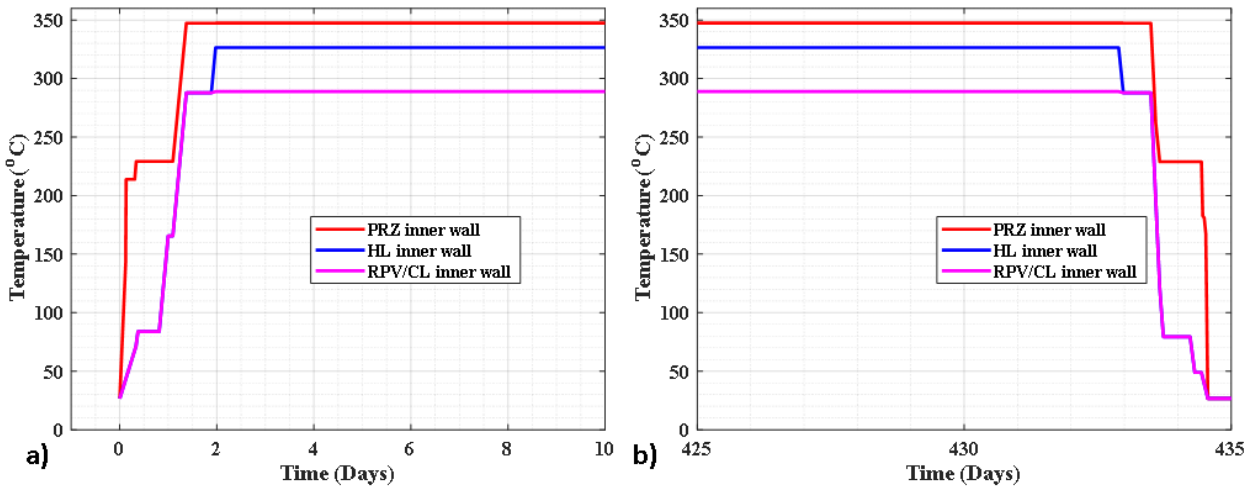

Figure 2. 4. Temperature-boundary conditions applied to the inner wall of PRZ, HL, RPV, and CL side of SG with magnified view during a) start and b) end of a design-basis fuel cycle.

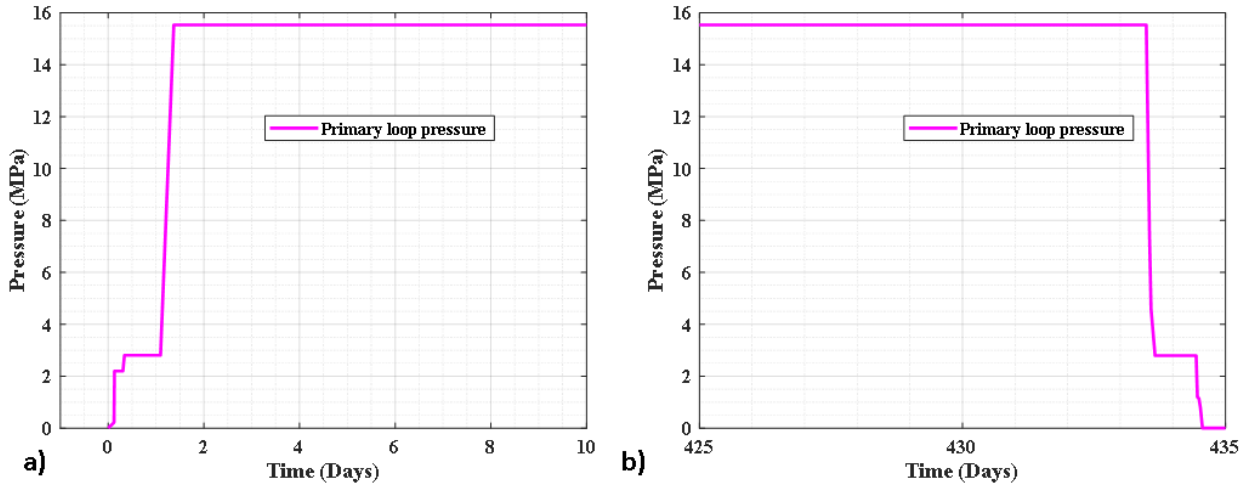

Figure 2. 5. Pressure boundary condition applied to the inner wall of PRZ, HL, RPV, HL, and CL side of SG with magnified view during a) start and b) end of a design-basis fuel cycle.

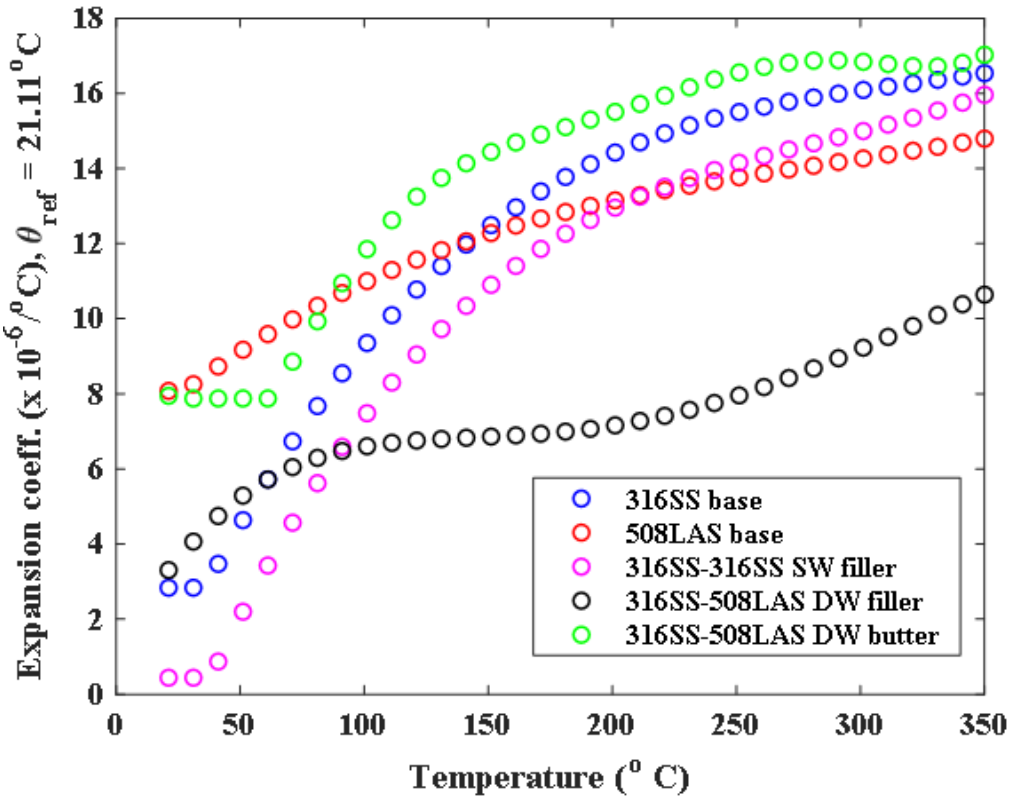

Figure 2. 6. Expansion coefficients for 316SS and 508LAS base, 316SS-316SS SW filler, and 316SS-508LAS DW filler and butter welds.

Table 2. 1 Tensile elastic-plastic properties used for 316SS base metal.

Temperature (°C)	Elastic modulus (GPa)	Poisson ratio	0.05% offset-strain yield stress (MPa)	Kinematic hardening parameter C1 (MPa)	Kinematic hardening parameter γ
22	175.1	0.27	217.41	13942	128.24
300	157.92	0.27	145.03	4373.5	33.25

Table 2. 2 Tensile elastic-plastic properties used for 316SS SMW-Filler Weld and 316SS Cladding.

Temperature (°C)	Elastic modulus (GPa)	Poisson ratio	0.05% offset-strain yield stress (MPa)	Kinematic hardening parameter C1 (MPa)	Kinematic hardening parameter γ
22	131.98	0.27	414.56	5901.8	65.922
300	129.11	0.27	345.8	4285.5	41.449

Table 2. 3 Tensile elastic-plastic properties used for 508 LAS base metal.

Temperature (°C)	Elastic modulus (GPa)	Poisson ratio	0.05% offset-strain yield stress (MPa)	Kinematic hardening parameter C1 (MPa)	Kinematic hardening parameter γ
22	209.72	0.27	494.36	2861.4	0
300	194.01	0.27	406.63	12240	57.768

Table 2. 4 Tensile elastic-plastic properties used for DMW-butter weld.

Temperature (°C)	Elastic modulus (GPa)	Poisson ratio	0.05% offset-strain yield stress (MPa)	Kinematic hardening parameter C1 (MPa)	Kinematic hardening parameter γ
22	149.7	0.27	387.64	9964.5	90.498
300	146.28	0.27	322	6307	64.861

Table 2. 5 Tensile elastic-plastic properties used for DMW-filler weld

Temperature (°C)	Elastic modulus (GPa)	Poisson ratio	0.05% offset-strain yield stress (MPa)	Kinematic hardening parameter C1 (MPa)	Kinematic hardening parameter γ
22	172.64	0.27	420.14	12023	99.532
300	196.57	0.27	359.72	6556.5	56.92

2.2 Theoretical Background: Fatigue Life Estimation Under Reactor Coolant Environment

Fatigue lives of RCS components were estimated based on the above-mentioned FE model simulated strain profiles and the NUREG-6909-based fatigue life estimation approach. The design life of a reactor component first needs to be estimated under an in-air environment by using the in-air design curve Then we must estimate the corresponding life under a reactor coolant environment by scaling the in-air life by using a scaling factor or environmental correction factor (F_{en}). Note that the mean curve is directly based on the test data and is the best-fit representation of the test data. However, because of scatter in test data (associated with material variability, surface finish, and size difference between test specimen and actual components), ASME code [9] suggests using the design curve to estimate the fatigue life of a component. The design curves are typically obtained based on the best fit or mean curves, by scaling the mean fatigue life by a factor of 20, for example, on life or fatigue cycles (as suggested by the ASME code). According to the ASME Code Section III, the factor of 20 has the following subfactors: (a) scatter of test data: 2.0, (b) specimen size effect: 2.5, and (c) specimen surface finish, subfactors: 4.0. Factors of 20 are not safety margins but rather adjustment factors that should be applied to the small-specimen data to obtain reasonable estimates of the lives of actual reactor components [2]. In this work, we estimated lives of the SS components and their nickel (Ni) -alloy-based welds (such as HL, SL, and their nozzles). For simplicity in this preliminary work, we used the same set of fatigue curves in the fatigue-life estimation of both the SS and Ni alloy welds. Note that with the absence of adequate data for constructing separate best fit (or mean) and design curves for alloy 600 and other Ni-Cr-Fe metals (including welds, for example, 82/182), NUREG-6909 [2] suggests using the strain versus in-air life ($\varepsilon \sim N_a$) curves of austenitic SS. However, for the proposed DT framework, the underlying software should be developed in such a way that can automatically identify the material type at any given 3D location (e.g., at thousands to millions of discretized FE nodes or elements) and use the appropriate fatigue life models. The generalization of the life estimation model will be one of our future works. Nevertheless, the above-mentioned scaling factor of 20 does not include the effect of a reactor coolant environment that could substantially reduce the life of a component. The NUREG-6909-based environmental correction factor (F_{en}) will further adjust the estimated design life of reactor components. Below are the NUREG-6909-based procedures to estimate the fatigue life of reactor components given a strain amplitude. The expression for the SS best fit or mean $\varepsilon \sim N_a$ curve for in-air condition can be given as:

$$\ln(N_a) = A - B\ln(\varepsilon - C) \tag{2.1}$$

In equation 2.1, ε and N_a respectively represent the strain amplitude and the corresponding in-air fatigue life, whereas A, B, and C are the fitting constants with values of 6.891, 1.920 and 0.112, respectively. Considering an environmental correction factor (F_{en}), the coolant-water environment life can be represented as:

$$N_w = \frac{N_a}{F_{en}} \tag{2.2}$$

Combining equations (2.1) and (2.2), the best fit or the mean curve under PWR-water environment is expressed as below:

$$\ln(N_w) = A - B\ln(\varepsilon - C) - \ln(F_{en}) \tag{2.3}$$

Note that in equation (2.3), A, B, and C are of the same fitting constants as the in-air curve since they are estimated based on in-air test data, whereas the environmental correction factor (F_{en}) must be estimated based on the fatigue-life data obtained under corresponding coolant-water environments. The details of the reasons and the methodology to estimate the above-mentioned parameters (e.g., A, B, C, and F_{en}) can be found in NUREG-6909 [2]. In the reported work, we considered a PWR so we can use the relevant PWR-coolant water environment F_{en}. Ideally, the $\varepsilon \sim N_a$ data and the expression representing the corresponding fatigue curve should be temperature dependent. However, according to NUREG-6909 [2], under in-air condition the SS grades (such as types 304, 304L, 316 and 316NG) do not show any significant effect on temperature up to 400°C. Hence, all the SS test data below 400°C are clubbed together to a single fatigue curve represented by equation. 2.1 with the same values of A, B, and C. In addition, under in-air condition and up to temperature of 400°C, there is not much strain rate effect for SS. However, under the PWR-water environment, the fatigue lives of SS and their Ni -alloy-based welds are not only dependent on temperature, but also on strain rate and dissolved oxygen concentration in the coolant water. The expression for F_{en} used in Eq. 2.3 is as below:

$$F_{en} = \exp\left(-T^*\dot{\varepsilon}^*O^*\right) \tag{2.4}$$

In equation (2.4), T*, ε*, and O* are transformed temperature, strain rate, and dissolved oxygen (DO), respectively. The transformed parameters used in the reported work (for both SS and their Ni-alloy-based weld components) are for Ni-Cr-Fe alloys. This is assuming that the existing environmental effect data for Ni-Cr-Fe alloys showed the same trends as those observed for austenitic SSs (also according to NUREG-6909 [2]). The details of the underlying data for these transformed parameters can be found from NUREG-6909 [2]. Nonetheless, the expressions for these transformed parameters are as follows:

$$\begin{aligned}
&T^* = 0;\ (T < 50°C)\\
&T^* = (T-50)/275;\ (50°C \le T \le 325°C)\\
&\varepsilon^* = 0\ ;\ (\dot{\varepsilon} > 5.0\%/s)\\
&\varepsilon^* = \ln(\dot{\varepsilon}/5.0);\ (0.0004\%/s \le \dot{\varepsilon} \le 5.0\%/s)\\
&\varepsilon^* = \ln(0.0004/5.0);\ (\dot{\varepsilon} < 0.0004\%/s)\\
&O^* = 0.14;\ (\text{PWR water, i.e., } < 0.1 \text{ ppm DO})
\end{aligned} \tag{2.5}$$

Inserting the expression for F_{en} from equation (2.4) into equation (2.3), the expression for the best-fit (or mean) strain amplitude versus life curve under PWR-water environment ($\varepsilon \sim N_w$) can be rewritten as below:

$$\ln(N_w) = A - B\ln(\varepsilon - C) + T^*\dot{\varepsilon}^*O^* \tag{2.6}$$

Using equations (2.1) and (2.6) and the strain amplitude estimated through the FE model, we can estimate the in-air and PWR-water design lives of RCS components. Note that for temperatures up to 400°C, although the in-air $\varepsilon \sim N_a$ curve is fixed, the corresponding water-environment curve does not remain the same but rather is dependent on temperature and the strain rate. Figure 2.7 shows the air best fit and the corresponding design curve with a scaling factor of 20 on cycles. Figure 2.7 also shows the PWR-water condition best-fit and design curve with a scaling factor of 20 on cycles. For the PWR-water curve, a strain rate of 0.0004%/s, a temperature of 325°C, and a dissolved-oxygen concentration of 5 parts per billion (ppb) (typical for a PWR primary water loop RCS component) were considered. The mentioned strain rate and temperature are the limiting values up to which the NUREG-6909-based F_{en} can be estimated. Note that RCS components of PWR experience a maximum temperature of 285–350°C. For all the reported fatigue life results, a strain rate of 0.0004%/s and temperature of 325°C are assumed up to which the equations (2.3–2.6) hold well. This is assuming that similar temperature and strain rate are also expected in an actual reactor. The strain rate of 0.0004%/s and temperature of 325°C can lead to an environmental correction factor F_{en} of 3.75, which is used for estimating all the PWR-water fatigue lives reported in this section (and for results reported in section 2.4). In addition, for all the reported fatigue life results (reported in this section), a limiting scaling factor of 20 on cycles was considered for scaling the in-air best fit or mean curve to the corresponding in-air design curve to find the worst-case fatigue lives. However, the actual fatigue life of a component can depend on the configuration/layout of the assembly of subcomponents investigated, the associated thermal-mechanical connected system boundary conditions, material cyclic hardening in each cycle, and the residual strain after each cycle. Also, in this work, only the SS and the Ni alloy region of the RCS components (such as HL, SL, and their nozzles) were evaluated. This is assuming that the LAS regions of the nozzles are not as vulnerable to fatigue because of their thicker section and associated lower stress states.

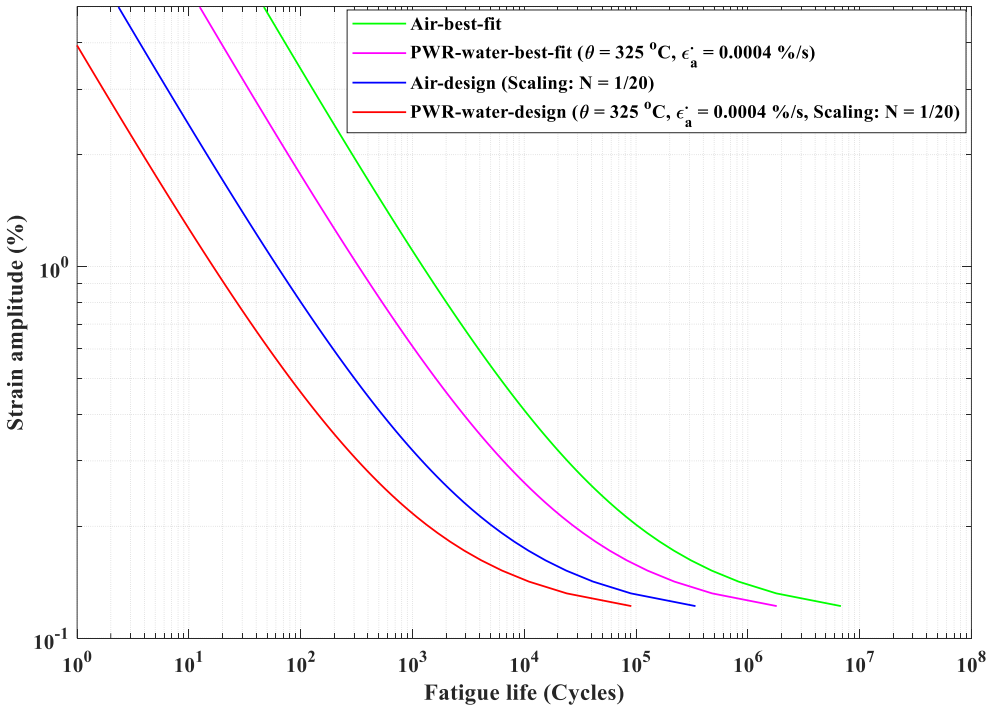

Figure 2. 7. Various strain versus life curves used for the life estimation of reported SS and Ni-alloy reactor components.

2.3 Estimated Component Strain Profile, Residual Strain and Fatigue Life Results

Based on the system-level-FE model (refer to section 2.1), thermal-mechanical stress analysis was performed for a design-basis loading cycle (refer to Figures 2.4 and 2.5). The subsection below describes the corresponding simulated strain amplitude and residual strain (after a single cycle) of major RCS components. Based on the estimated strain profile, we estimated the lives of the RCS components. Although the system-level boundary conditions were simulated considering RPV, PRZ, SG, HL, and SL [5] in the discussed work, only the HL, SL, and their nozzles were evaluated as example components.

2.3.1 Strain Profile of HL-Side Nozzle of SL and the Corresponding Fatigue life

Based on the system-level stress analysis model, we estimated various strain profiles of the HL-side nozzle of SL (see Figure 2.3). Figure 2.8 shows the temperature versus maximum principal total and thermal strain at the DMW region of the nozzle. Figure 2.9 shows the corresponding temperature versus equivalent mechanical strain profile, whereas Figure 2.10 shows the temperature versus multi-axial-equivalent or von-Mises stress at the DMW region of the HL-side-nozzle of SL. Note that equivalent mechanical strain is the effective strain or the result of all the mechanical strain components, whereas the mechanical strain components are the difference of the corresponding total and thermal strain components. The resulting equivalent strain is the uniaxial representation of all the mechanical strain components. Also, the strain versus life ($\varepsilon \sim N$) curves are constructed based on the uniaxial fatigue test data, with tests conducted under strain-control (essentially the mechanical strain-control) conditions. Hence, to use the $\varepsilon \sim N$ curves for fatigue evaluation, the FE-simulated total and thermal-strain components first need to be transferred to the corresponding equivalent mechanical strain. Similar to the DMW region of the HL-side nozzle of SL, results are also plotted at the SS transition (between DMW and SMW) region of the HL-side nozzle of SL. For example, Figure 2.11 shows the corresponding temperature versus maximum principal total and thermal strain. Whereas Figures 2.12 and 2.13 show the corresponding temperature versus multi-axial-equivalent mechanical strain and multi-axial-equivalent or von-Mises stress, respectively. All the above-mentioned strain or stress profiles show the variation of strain amplitude during heat-up, steady-state power operation, and cool-down of the reactor fuel cycle (see Figures 2.4 and 2.5).

The corresponding strain amplitudes, residual strain, and the fatigue lives are summarized in Table 2.6. The equivalent or von Mises stress amplitude and the corresponding residual (at the end of the fuel cycle) values can also be found in Table 2.6. As seen in Table 2.6, the DMW region of the HL-side nozzle of SL experiences mechanical-strain amplitude and residual of 0.248% and 0.204%, respectively. In further cycling, the strain amplitude and the residual strain may change due to the combined effect of cyclic hardening and environmental effect. Nevertheless, these results show that the DMW region of the nozzle does not return to the original strain states (i.e., at the start of the reactor) and with significant residual strain of 0.204%. Although it was originally thought the DMW region of the nozzle would experience the highest strain, results show it does not. Rather, the adjacent SS transition (between DMW and SMW) experiences a higher strain amplitude and residual of 0.836% and 1.34%, respectively. Although the overall structural integrity of the HL-side nozzle depends on all the LAS, SS, DMW, and SMW regions of HL-side nozzle, the SS transition (between DMW and SMW) region shows the highest strain (both amplitude and residual). The crack in this region can initiate faster than other regions. For that

reason, more focused/detailed NDE must be done at the SS transition region of HL-side nozzle compared to other RCS components as found in succeeding results.

The fatigue life of the overall component was assumed to be the lowest fatigued lives estimated for different regions. The fatigue lives of the DMW and SS transition regions were estimated by considering mean and limiting design fatigue curves (Section 2.2 and Figure 2.7). The fatigue lives were also estimated under in-air and PWR-water environment. From Table 2.6, the best case (based on mean curve data) and worse case (based on design curve data) PWR-water-fatigue-life of HL-side nozzle can be 493 and 25 cycles, respectively. These results are representative. The actual life of a particular component can depend on the actual geometry of the component and the plant layout, which governs the connected system thermal-mechanical boundary conditions. Nevertheless, these results show the importance of a system-level model to predict the stress-strain states and lives of a component more accurately, rather than depending on a single-component based simulation models.

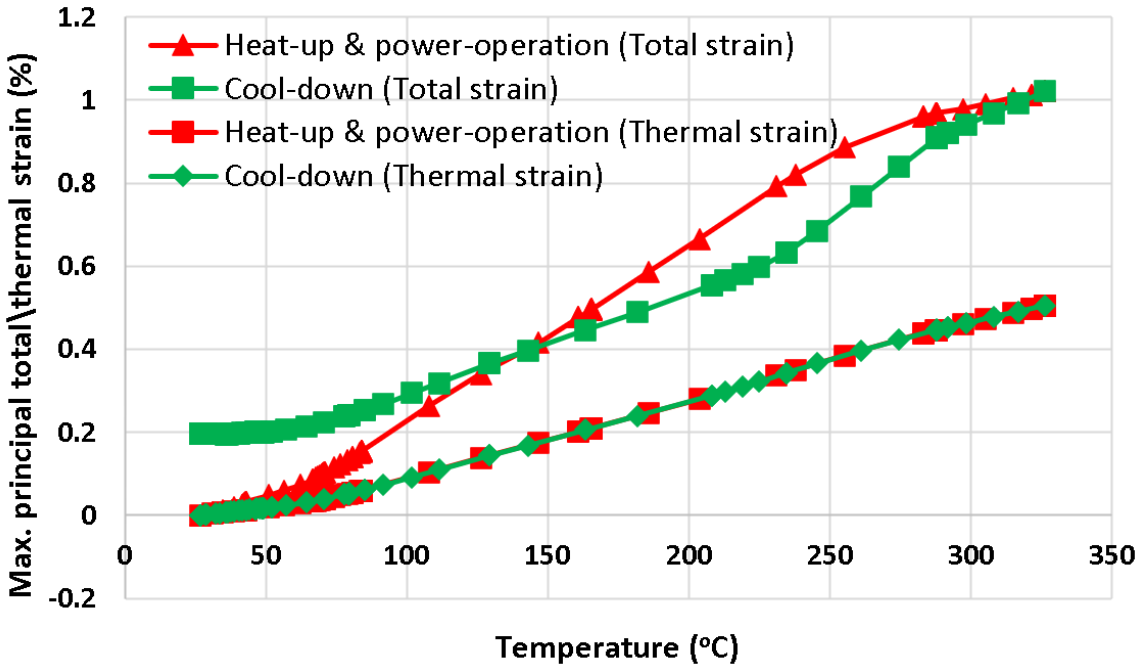

Figure 2. 8. Temperature versus maximum principal total and thermal strain at the DMW region of the HL-side nozzle of SL.

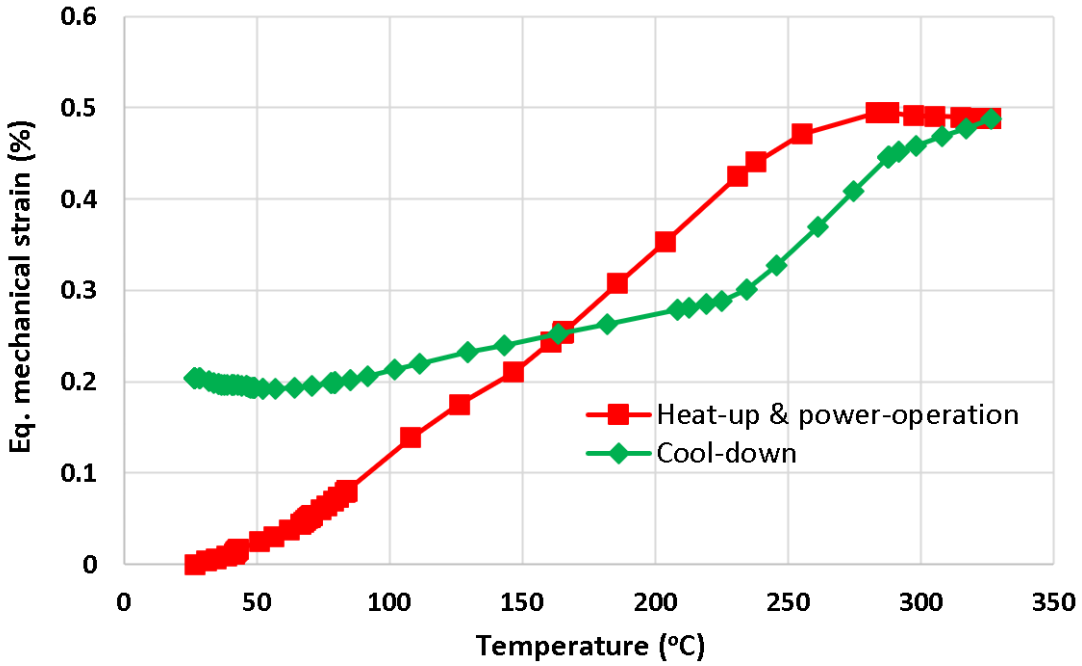

Figure 2. 9. Temperature versus multi-axial-equivalent mechanical strain at the DMW region of the HL-side nozzle of SL.

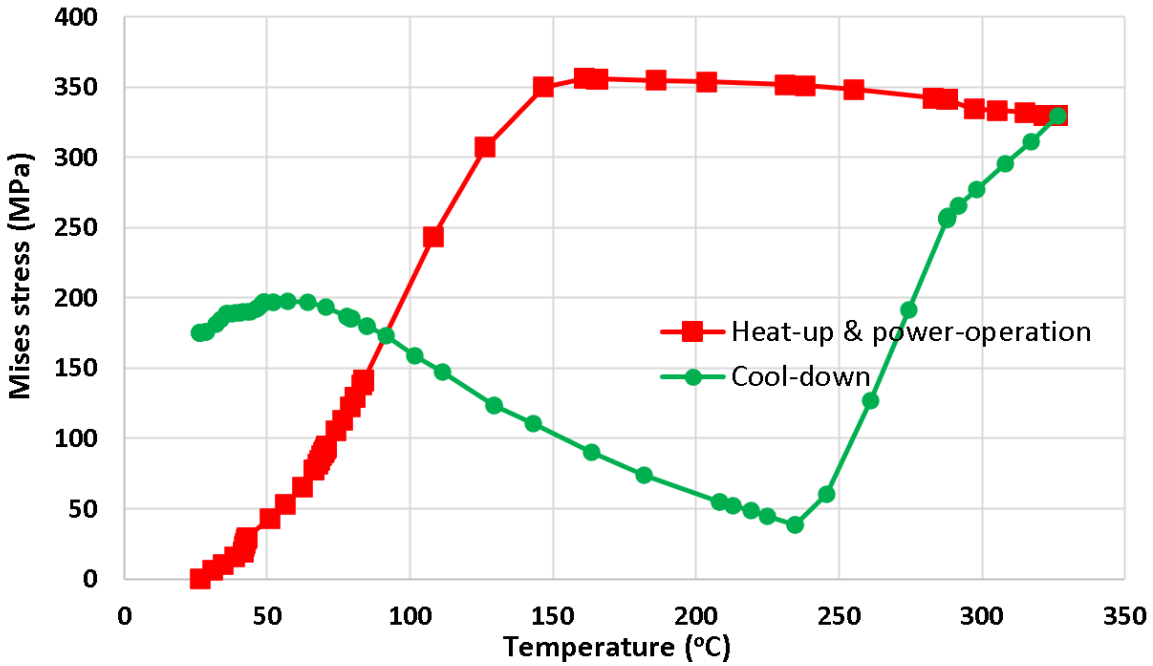

Figure 2. 10. Temperature versus multi-axial-equivalent or Von-Mises stress at the DMW region of the HL-side-nozzle of SL.

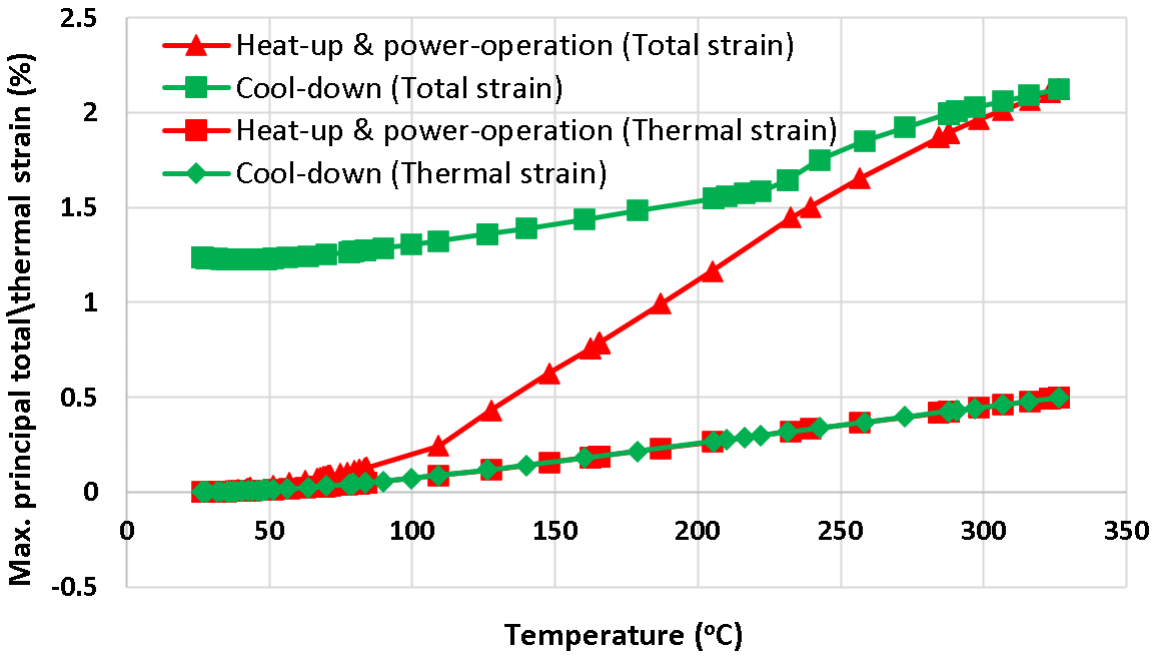

Figure 2. 11. Temperature versus maximum principal total and thermal strain at the SS transition (between DMW and SMW) region of the HL-side-nozzle of SL.

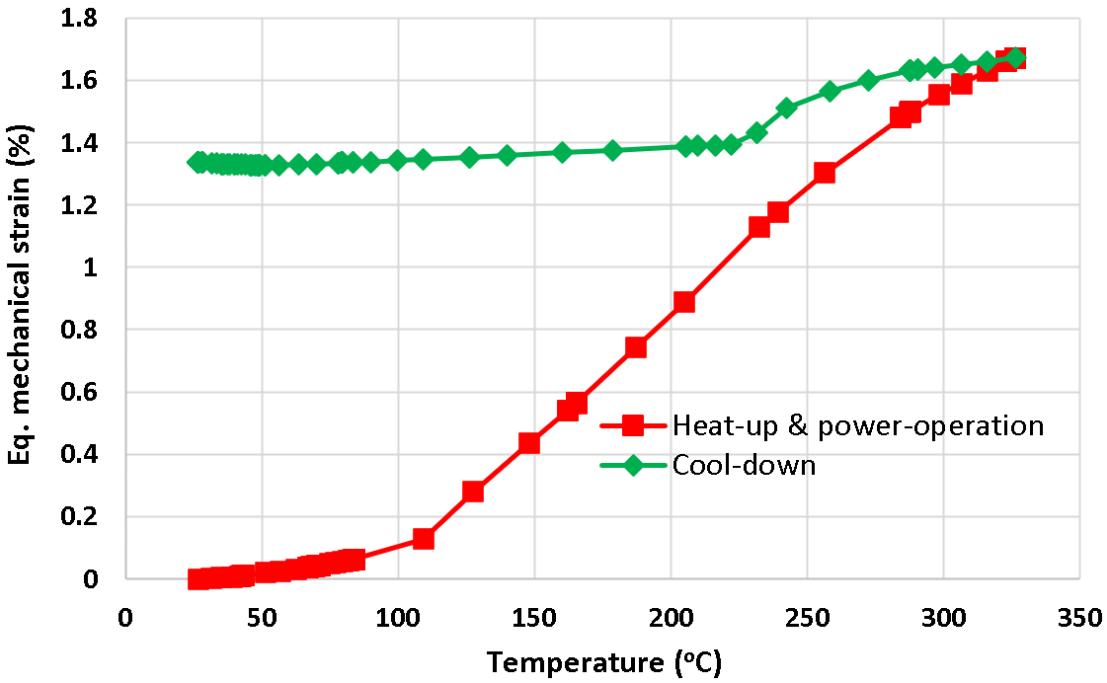

Figure 2. 12. Temperature versus multi-axial-equivalent mechanical strain at the SS transition (between DMW and SMW) region of the HL-side nozzle of SL.

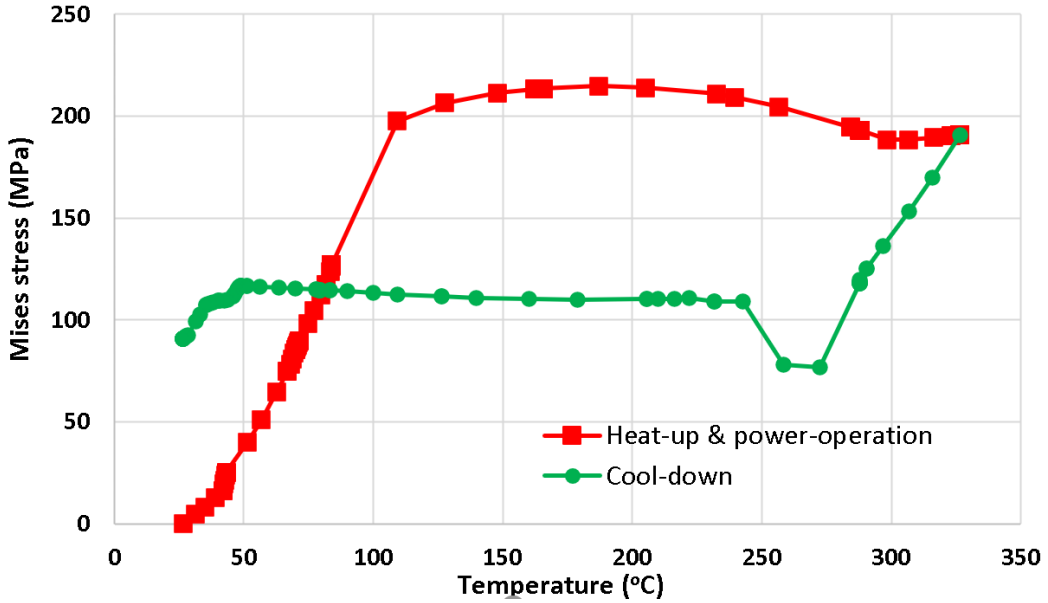

Figure 2. 13. Temperature versus multi-axial-equivalent or Von-Mises stress at the SS transition (between DMW and SMW) region of the HL-side-nozzle of SL.

Table 2. 6. Summary of various strain, stress amplitudes and estimated of HL-side nozzle of SL.

Parameters	DMW region	⊗Non-DMW region
Max. of max. principal total strain range (%)	1.021	2.125
Max. of max. principal thermal strain range (%)	0.505	0.498
Max. of equivalent mechanical strain range (%)	0.495	1.672
Max. of equivalent mechanical strain amplitude (%)	**0.248**	**0.836**
Max. of von Mises stress amplitude (MPa)	356	215
Residual equivalent mechanical strain after 1st cycle (%)	**0.204**	**1.34**
Residual equivalent (von Mises) stress after 1st cycle (MPa)	175	91
Mean in-air life, N_a (cycles)	49,426	1848
Design in-air life, $N_d = \left(\frac{1}{20}\right) * N_a$ (cycles)	2,471	92
F_{en}	3.75	
Mean PWR water life, $N_w = \left(\frac{1}{Fen}\right) * N_a$ (cycles)	13,180	493
Design PWR water life, $N_{w,d} = \left(\frac{1}{Fen}\right) * N_d$ (cycles)	659	25
Best case scenario: Mean PWR water life i.e., minimum N_w of all regions (cycles)	**493**	
Worst case scenario: Minimum possible PWR water life i.e.., minimum $N_{w,d}$ of all regions (cycles)	**25**	

⊗Non-DMW region controlling the fatigue life, in this case the SS transition between DMW and SMW.

2.3.2 Strain Profile of PRZ-Side Nozzle of SL and the Corresponding Fatigue Life

Figure 2.14 shows the temperature versus maximum principal total and thermal strain at the DMW region of the PRZ-side-nozzle of SL. The corresponding equivalent mechanical strain and stress (von Mises stress) are shown in Figures 2.15 and 2.16, respectively. Table 2.7 shows the corresponding summary of various strain, stress amplitudes, and fatigue lives. Comparing Figure 2.15 with Figure 2.9, the DMW region of the PRZ-side nozzle of SL experiences significantly lower strain compared to the corresponding DMW region of the HL-side nozzle of SL, even though both nozzles have the same geometry and material properties. The variation of strain is primarily due to connected system thermal-mechanical boundary conditions and lower temperature at the HL-side nozzle (maximum temperature is approximately 326.4°C) compared to the temperature at the PRZ-side nozzle (maximum temperature is approximately 347.3°C). The connected-system thermal-mechanical boundary conditions of the PRZ-side nozzle of SL led to almost elastic cycling and nearly zero residual strain and stress after the first cycle. Accordingly, the PWR-water life of the PRZ-side nozzle can be significantly higher than the corresponding HL-side nozzle and probably does not need as significant NDE-based scrutinizing as does the HL-side nozzle.

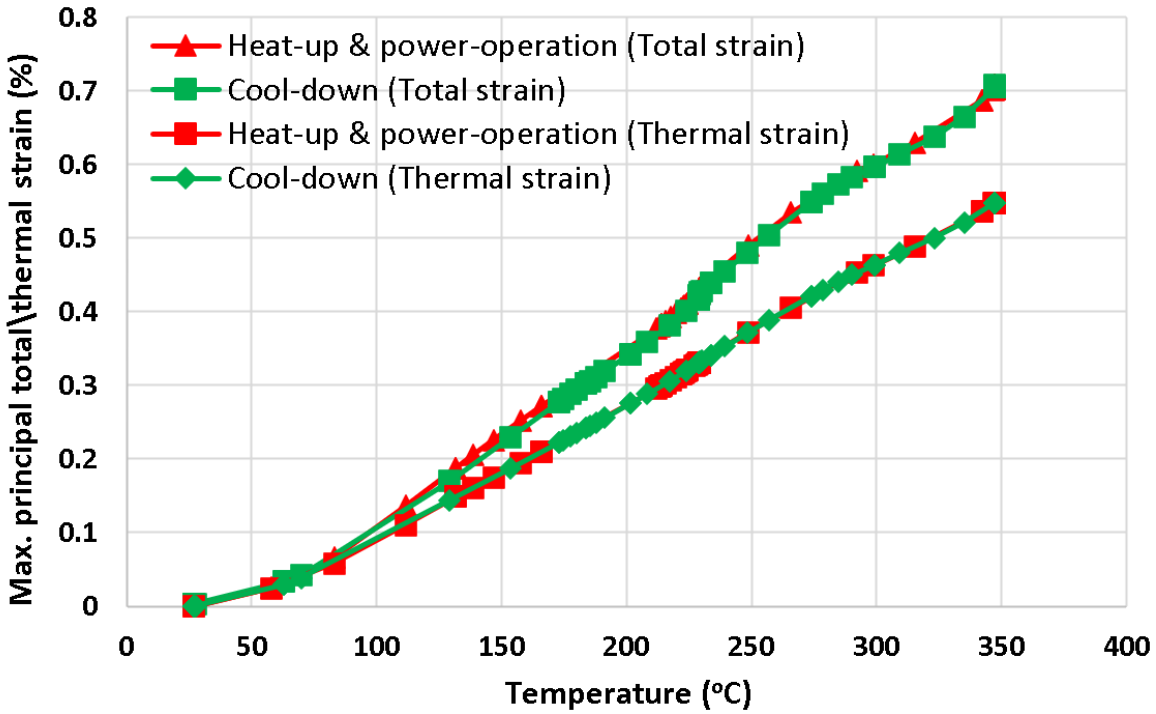

Figure 2. 14. Temperature versus maximum principal total and thermal strain at the DMW region of the PRZ-side-nozzle of SL.

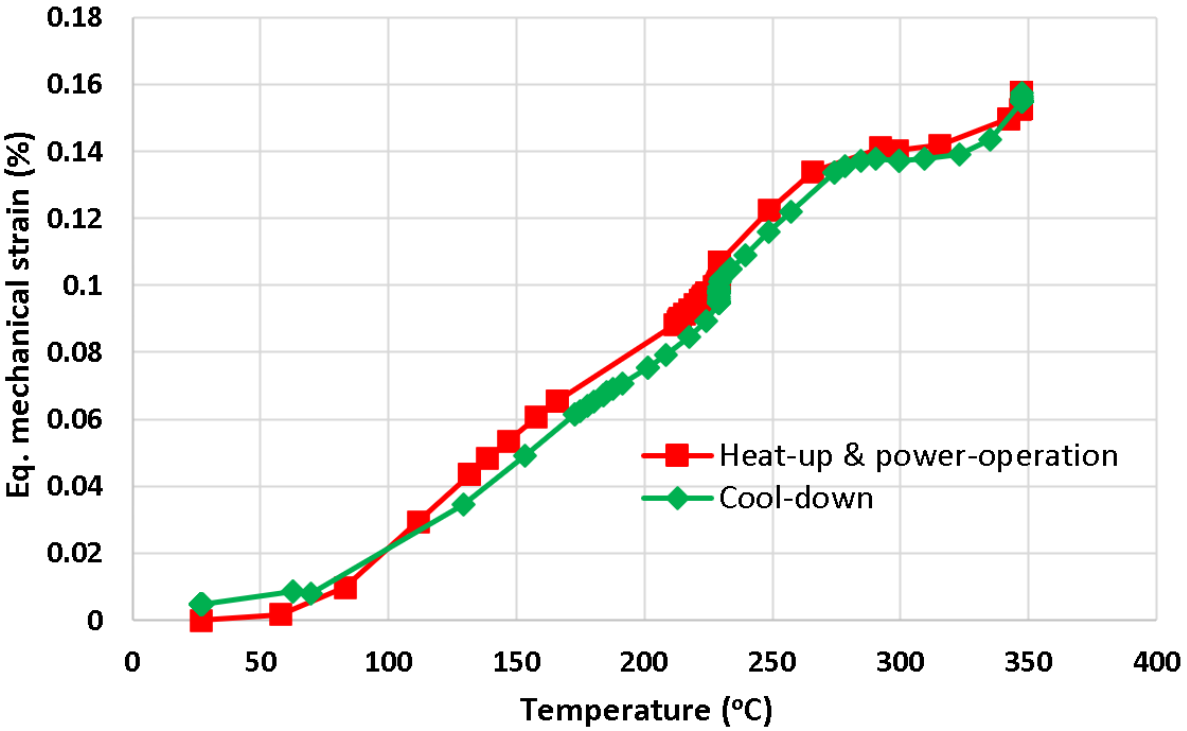

Figure 2. 15. Temperature versus multi-axial-equivalent mechanical strain at the DMW region of the PRZ-side nozzle of SL.

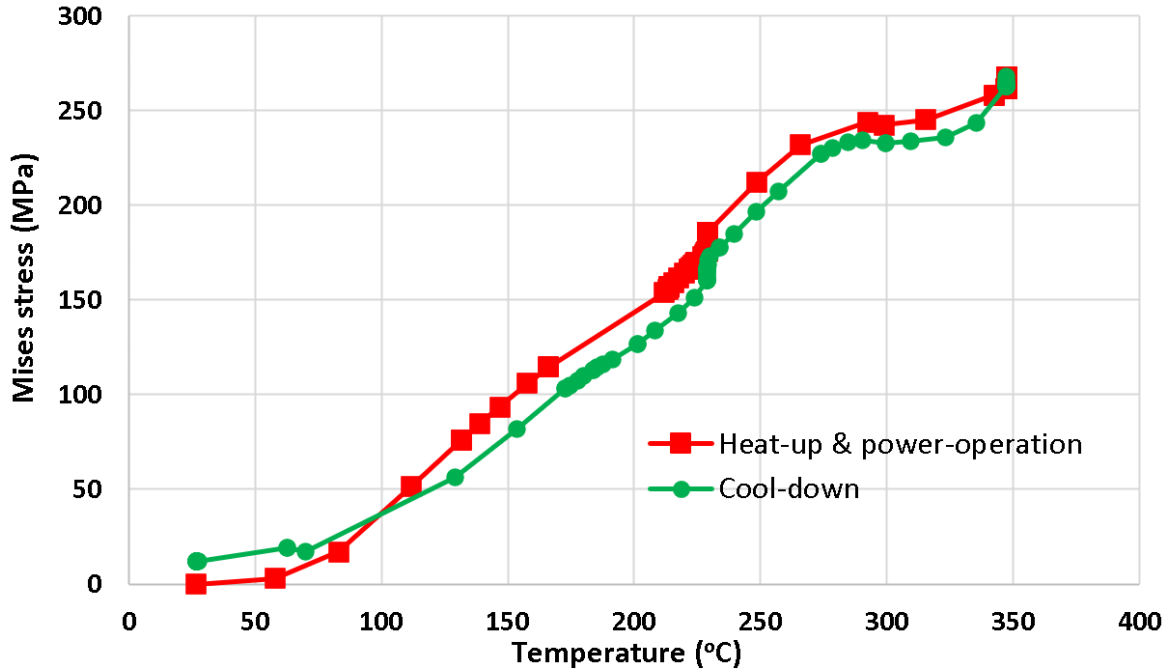

Figure 2. 16. Temperature versus multi-axial-equivalent or Von-Mises stress at the DMW region of the PRZ-side-nozzle of SL.

Table 2. 7. Summary of various strain, stress amplitudes and life of PRZ-side nozzle of SL.

Parameters	DMW region	⊗Non-DMW region
Max. of max. principal total strain range (%)	0.708	NA
Max. of max. principal thermal strain range (%)	0.548	NA
Max. of equivalent mechanical strain range (%)	0.157	NA
Max. of equivalent mechanical strain amplitude (%)	**0.079**	NA
Max. of von Mises stress amplitude (MPa)	268	NA
Residual equivalent mechanical strain after 1st cycle (%)	**0.005**	NA
Residual equivalent (von Mises) stress after 1st cycle (MPa)	12	NA
Mean in-air life, N_a (cycles)	>1e6	NA
Design in-air life, $N_d = \left(\frac{1}{20}\right) * N_a$ (cycles)	>1e5	NA
F_{en}	3.75	
Mean PWR water life, $N_w = \left(\frac{1}{Fen}\right) * N_a$ (cycles)	>1e6	NA
Design PWR water life, $N_{w,d} = \left(\frac{1}{Fen}\right) * N_d$ (cycles)	>1e5	NA
Best case scenario: Mean PWR water life i.e., minimum N_w of all regions (cycles)	**>1e6**	
Worst case scenario: Minimum possible PWR water life, i.e., minimum $N_{w,d}$ of all regions (cycles)	**>1e5**	

2.3.3 Strain Profile of SS Base Pipe of SL and the Corresponding Fatigue Life

Figure 2.17 shows the temperature versus maximum principal total and thermal strain at the SS base pipe region of SL. Whereas, Figures 2.18 and 2.19 show the corresponding multi-axial equivalent mechanical strain and stress (von. Mises stress) profiles of the SL, which is made from SS metal only. Table 2.8 shows the corresponding summary of various strain- stress amplitudes and fatigue lives. Table 2.8 shows that the SL pipe experiences a maximum strain amplitude of 0.182% and residual strain of 0.25% (after the 1st cycle), which shows a significant shift in mean strain. Nevertheless, the worst possible PWR-water life of SL pipe can be 2,163 cycles.

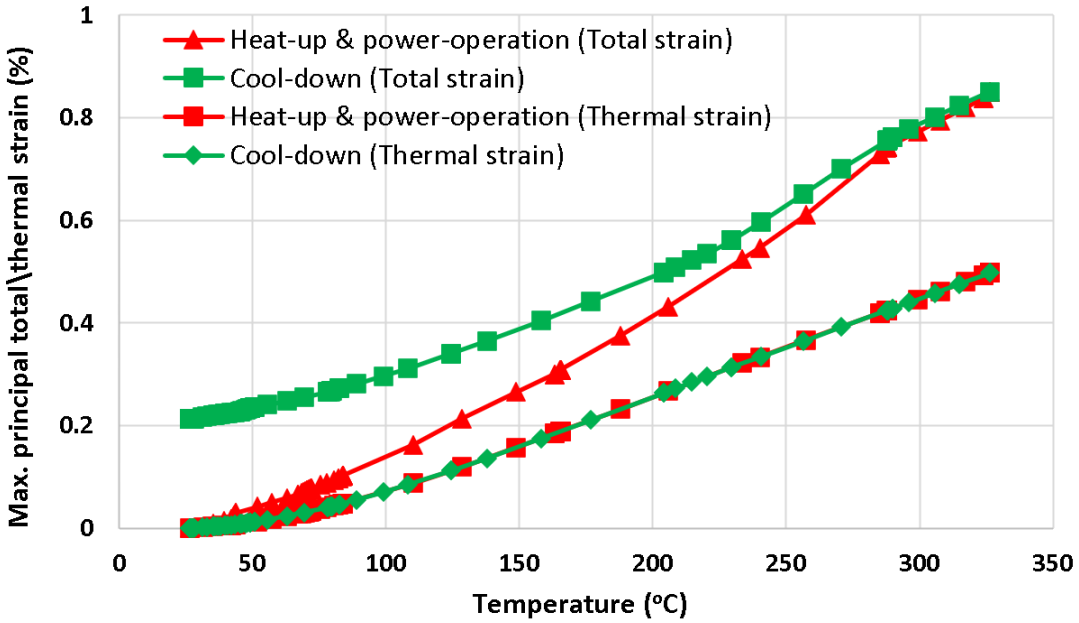

Figure 2. 17. Temperature versus maximum principal total and thermal strain at the SS base pipe region of SL.

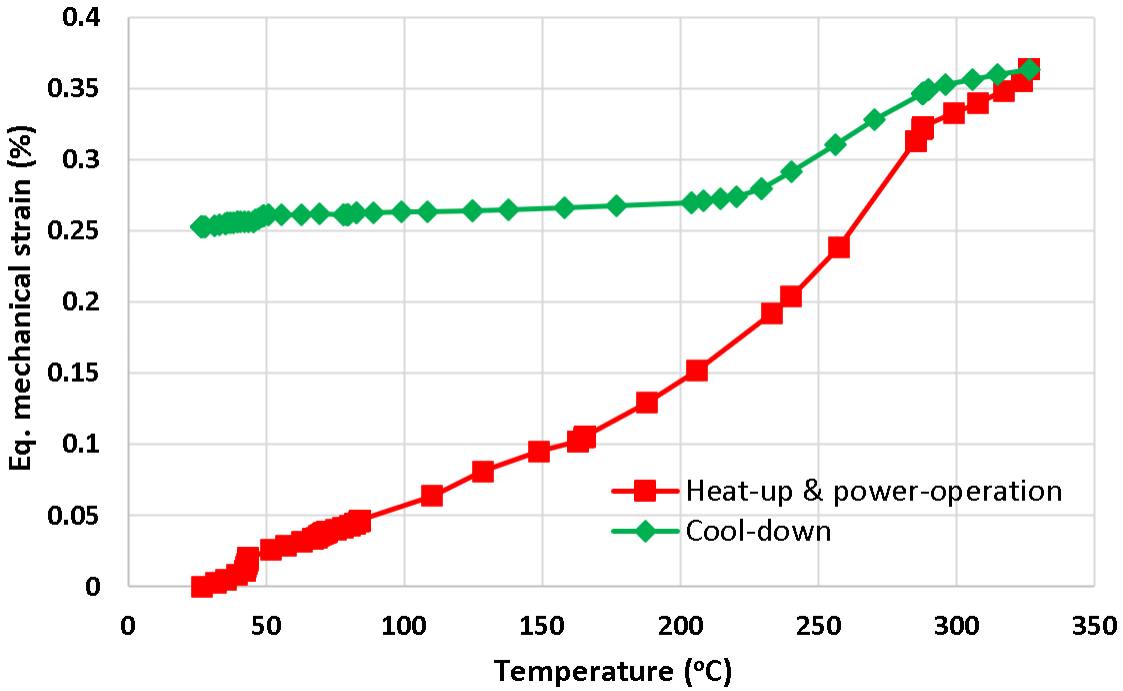

Figure 2. 18. Temperature versus multi-axial-equivalent mechanical strain at the SS base pipe region of SL.

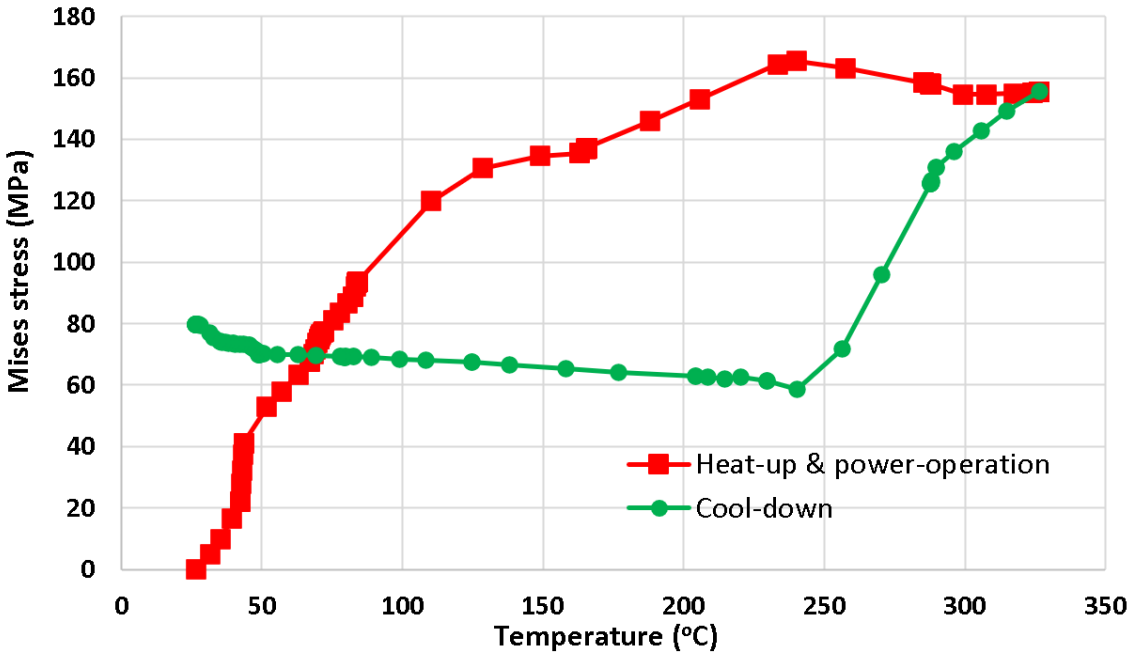

Figure 2. 19. Temperature versus multi-axial-equivalent or Von-Mises stress at the SS base pipe region of SL.

Table 2. 8. Summary of various strain, stress amplitudes, and life of SS base pipe region of SL.

Parameters	SS base pipe region of SL
Max. of max. principal total strain range (%)	0.851
Max. of max. principal thermal strain range (%)	0.498
Max. of equivalent mechanical strain range (%)	0.363
Max. of equivalent mechanical strain amplitude (%)	**0.182**
Max. of von Mises stress amplitude (MPa)	165
Residual equivalent mechanical strain after 1st cycle (%)	**0.25**
Residual equivalent (von Mises) stress after 1st cycle (MPa)	80
Mean in-air life (N_a), cycles	162,231
Design in-air life ($N_d = \left(\frac{1}{20}\right) * N_a$), cycles	8,112
F_{en}	3.75
Mean PWR water life ($N_w = \left(\frac{1}{Fen}\right) * N_a$), cycles	43,262
Design PWR water life ($N_{w,d} = \left(\frac{1}{Fen}\right) * N_d$), cycles	2,163
Best case scenario: Mean PWR water life (minimum N_w of all regions), cycles	**43,262**
Worst case scenario: Minimum possible PWR water life (minimum $N_{w,d}$ of all regions), cycles	**2,163**

2.3.4 Strain Profile of RPV-Side Nozzle of HL and the Corresponding Fatigue Life

Figure 2.20 shows the temperature versus maximum principal total and thermal strain at the DMW region of the RPV-side-nozzle of HL. The corresponding multi-axial-equivalent mechanical strain and von Mises stress profiles are shown in Figures 2.21 and 2.22, respectively, whereas Figure 2.23 shows the temperature versus maximum principal total and thermal strain at the SS transition (between DMW and SMW) region of the RPV-side-nozzle of HL. The corresponding multi-axial-equivalent mechanical strain and von Mises stress profiles are shown in Figures 2.24 and 2.25, respectively. Table 2.9 shows the corresponding summary of various strain, stress amplitudes, and fatigue lives. From the table and figures, the SS transition region is more vulnerable than the DMW region. For example, the SS transition region of RPV-side nozzle experiences a maximum strain amplitude of 0.457%, which is significantly higher than the DMW region. However, as shown in Table 2.9, despite a higher strain amplitude, the SS transition region experiences similar residual strain after the first cycle as the DMW region. Unless a system-level model is used (contrary to the conventional single component level model), accurate quantification of the stress-strain states of individual regions (under connected component thermal-mechanical boundary conditions) is difficult. Nevertheless, the worst possible PWR-water life of RPV-side nozzle of HL can be found as 98 cycles.

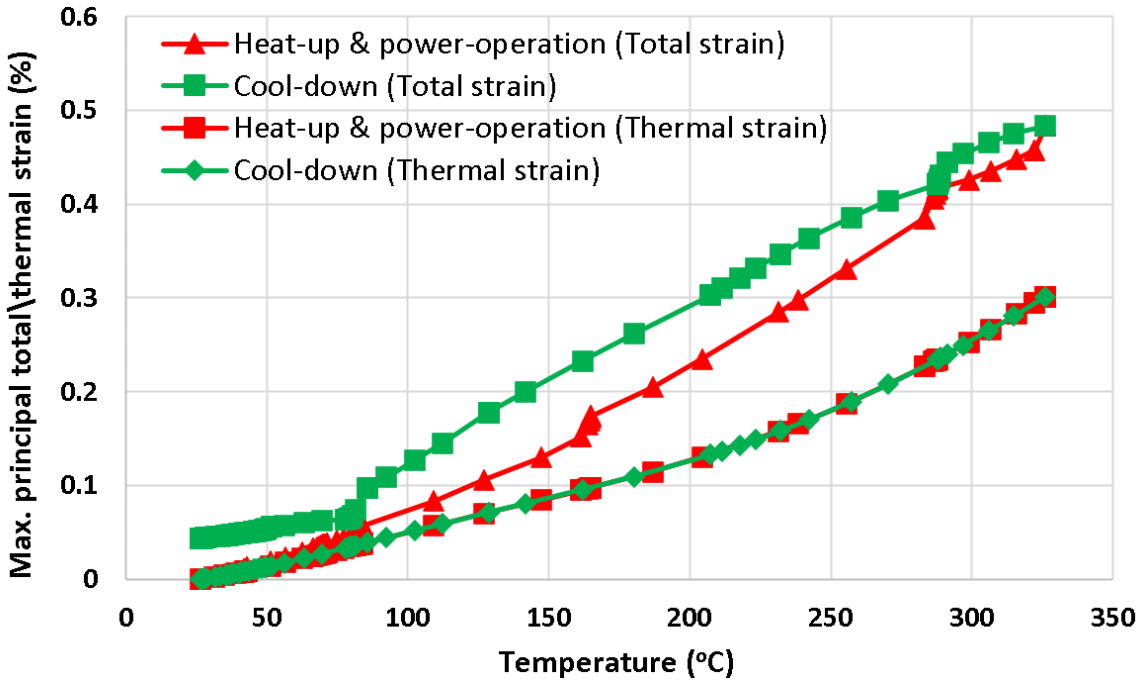

Figure 2. 20. Temperature versus maximum principal total and thermal strain at the DMW region of the RPV-side-nozzle of HL.

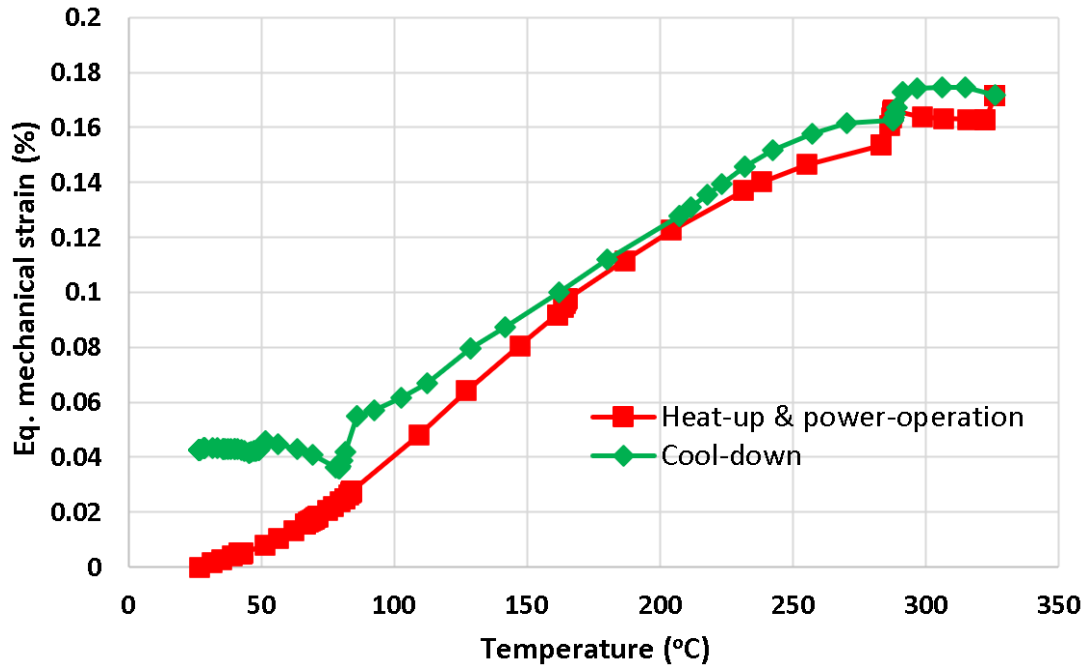

Figure 2. 21. Temperature versus multi-axial-equivalent mechanical strain at the DMW region of the RPV-side-nozzle of HL.

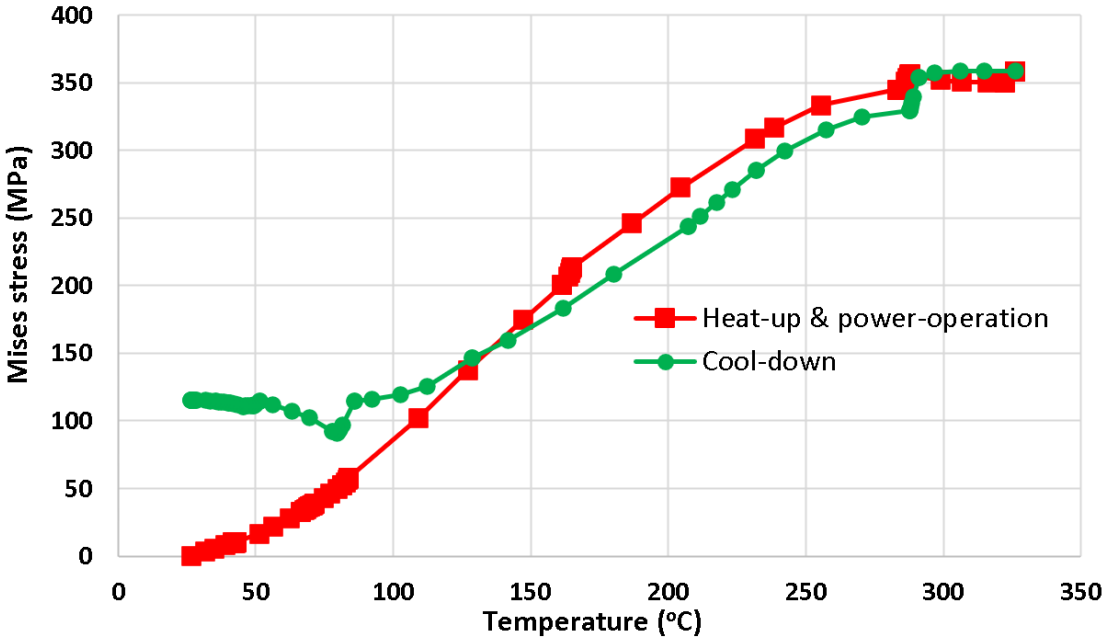

Figure 2. 22. Temperature versus multi-axial-equivalent or Von-Mises stress at the DMW region of the RPV-side-nozzle of HL.

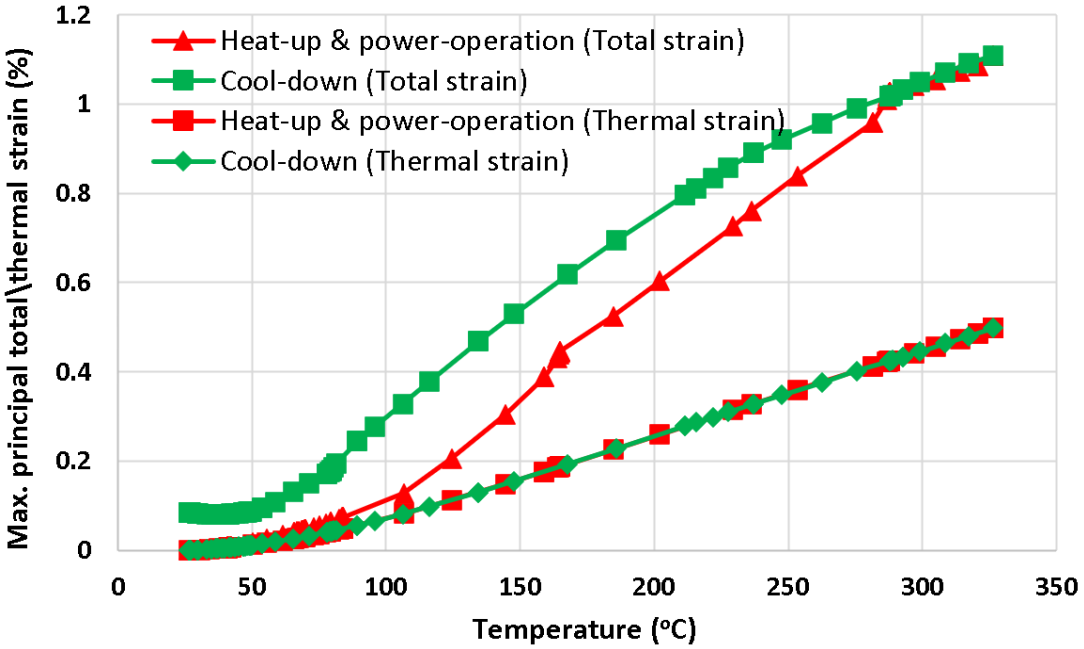

Figure 2. 23. Temperature versus maximum principal total and thermal strain at the SS transition (between DMW and SMW) region of the RPV-side-nozzle of HL.

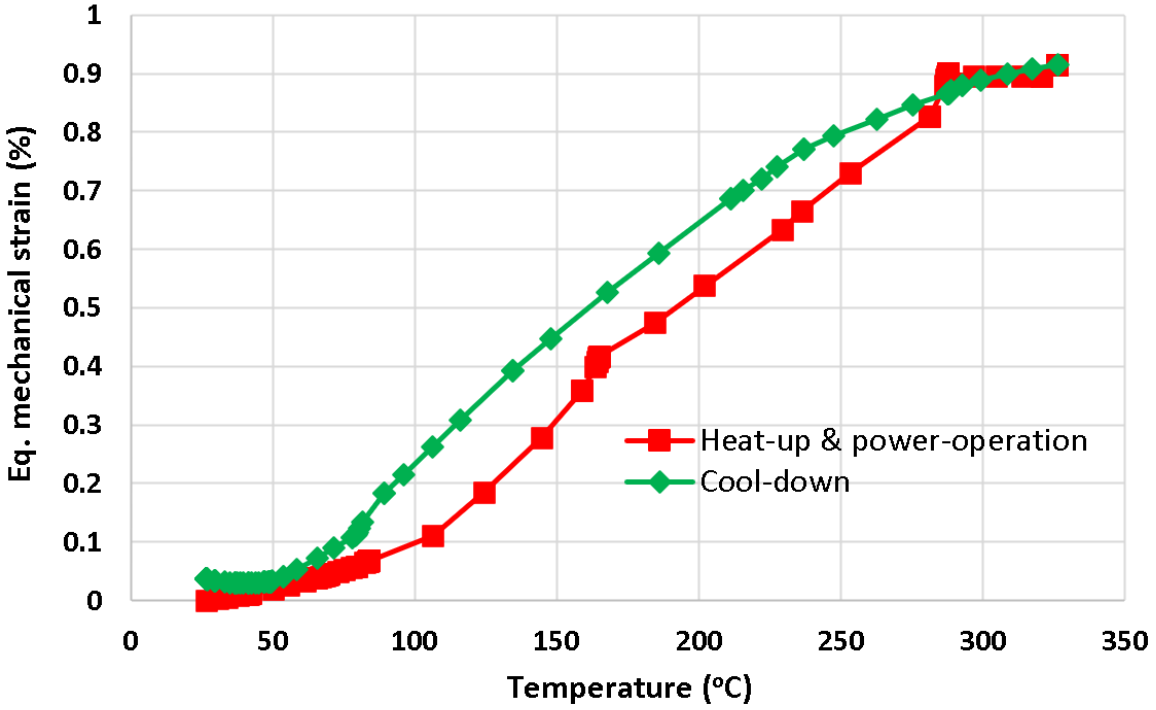

Figure 2. 24. Temperature versus multi-axial-equivalent mechanical strain at the SS transition (between DMW and SMW) region of the RPV-side-nozzle of HL.

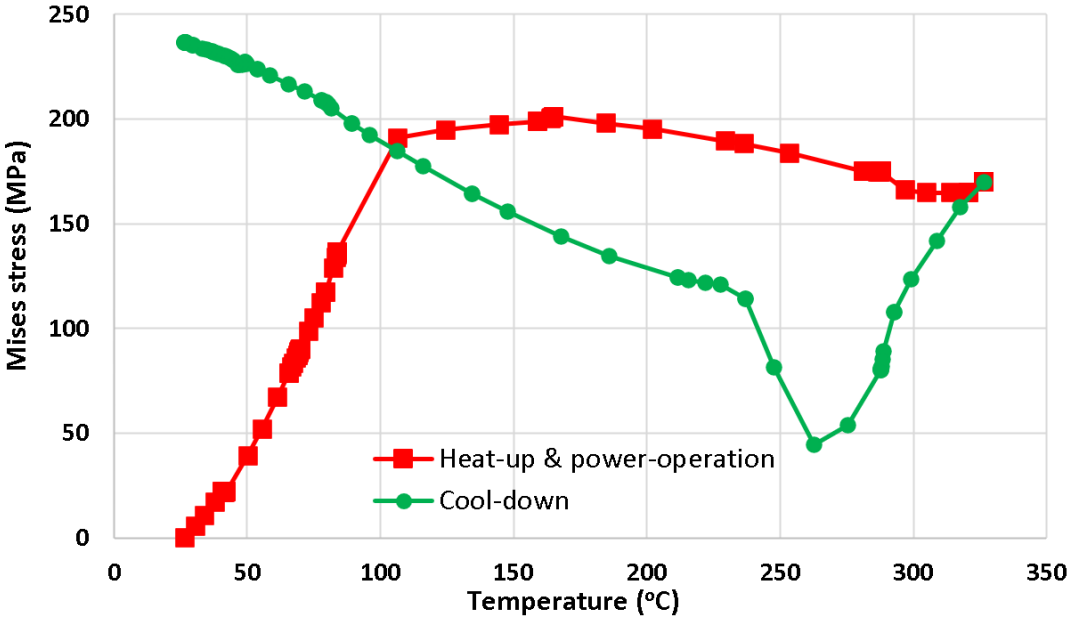

Figure 2. 25. Temperature versus multi-axial-equivalent or Von-Mises stress at the SS transition (between DMW and SMW) region of the RPV-side-nozzle of HL.

Table 2. 9. Summary of various strain, stress amplitudes and estimated of RPV-side nozzle of HL.

Parameters	DMW region	⊗Non-DMW region
Max. of max. principal total strain range (%)	0.483	1.110
Max. of max. principal thermal strain range (%)	0.301	0.498
Max. of equivalent mechanical strain range (%)	0.175	0.914
Max. of equivalent mechanical strain amplitude (%)	**0.088**	**0.457**
Max. of von Mises stress amplitude (MPa)	359	237
Residual equivalent mechanical strain after 1st cycle (%)	**0.043**	**0.033**
Residual equivalent (von Mises) stress after 1st cycle (MPa)	115	237
Mean in-air life, N_a (cycles)	>1e6	7381
Design in-air life, $N_d = \left(\frac{1}{20}\right) * N_a$ (cycles)	>1e5	369
F_{en}	3.75	
Mean PWR water life, $N_w = \left(\frac{1}{Fen}\right) * N_a$ (cycles)	>1e6	1968
Design PWR water life, $N_{w,d} = \left(\frac{1}{Fen}\right) * N_d$ (cycles)	>1e5	98
Best case scenario: Mean PWR water life i.e., minimum N_w of all regions (cycles)	**1968**	
Worst case scenario: Minimum possible PWR water life i.e., minimum $N_{w,d}$ of all regions (cycles)	**98**	

⊗Non-DMW region controlling the fatigue life, in this case the SS transition between DMW and SMW.

2.3.5 Strain Profile of SG-Side Nozzle of HL and the Corresponding Fatigue Life

Figure 2.26 shows the temperature versus maximum principal total and thermal strain at the DMW region of the SG-side-nozzle of HL. The corresponding multi-axial-equivalent mechanical strain and von Mises stress profiles are shown in Figures 2.27 and 2.28, respectively, whereas Figure 2.29 shows the temperature versus maximum principal total and thermal strain at the LAS transition (between DMW and SG) region of the SG-side-nozzle of HL. The corresponding multi-axial-equivalent mechanical strain and von Mises stress profiles are shown in Figures 2.30 and 2.31, respectively. Table 2.10 shows the corresponding summary of various strain, stress amplitudes, and fatigue lives. From Figure 2.27, the DMW region of SG-side nozzle of HL mostly experiences elastic deformation without much residual strain. Nevertheless, both RPV-side and SG-side nozzles of HL have the same geometry and are subjected to similar temperature and pressure profiles. The SG-side nozzle can experience significantly lower strain amplitude than the RPV-side nozzle. Accordingly, unlike the RPV-side nozzle, the SG-side nozzle of HL can have significantly higher fatigue life and may not require frequent and detailed NDE inspections.

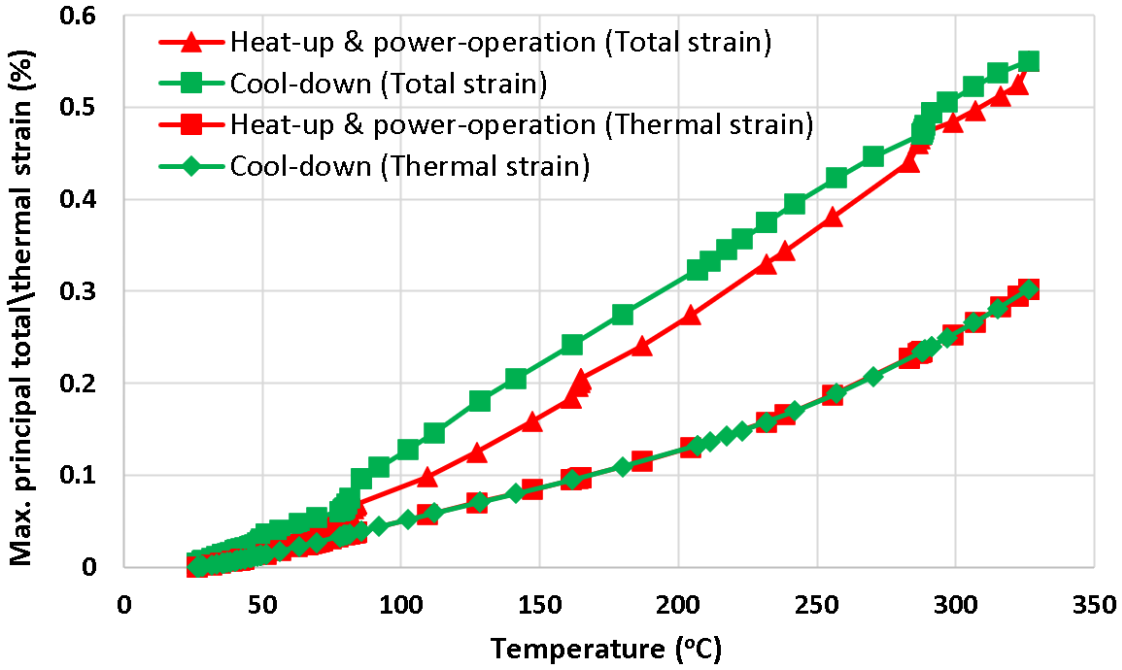

Figure 2. 26. Temperature versus maximum principal total and thermal strain at the DMW region of the SG-side-nozzle of HL.

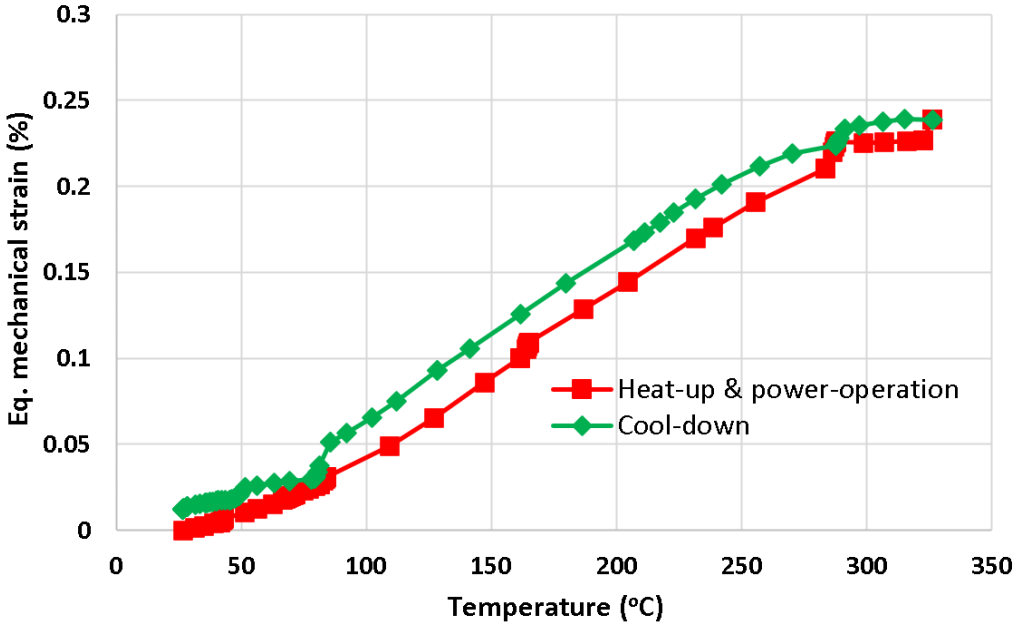

Figure 2. 27. Temperature versus multi-axial-equivalent mechanical strain at the DMW region of the SG-side-nozzle of HL.

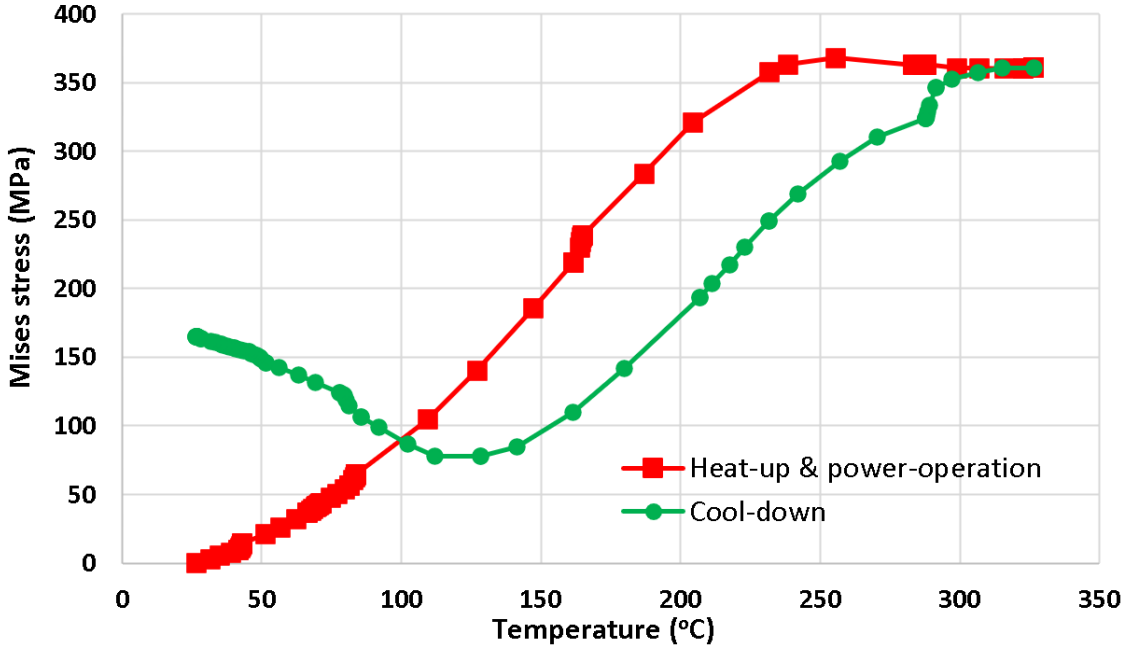

Figure 2. 28. Temperature versus multi-axial-equivalent or Von-Mises stress at the DMW region of the SG-side-nozzle of HL.

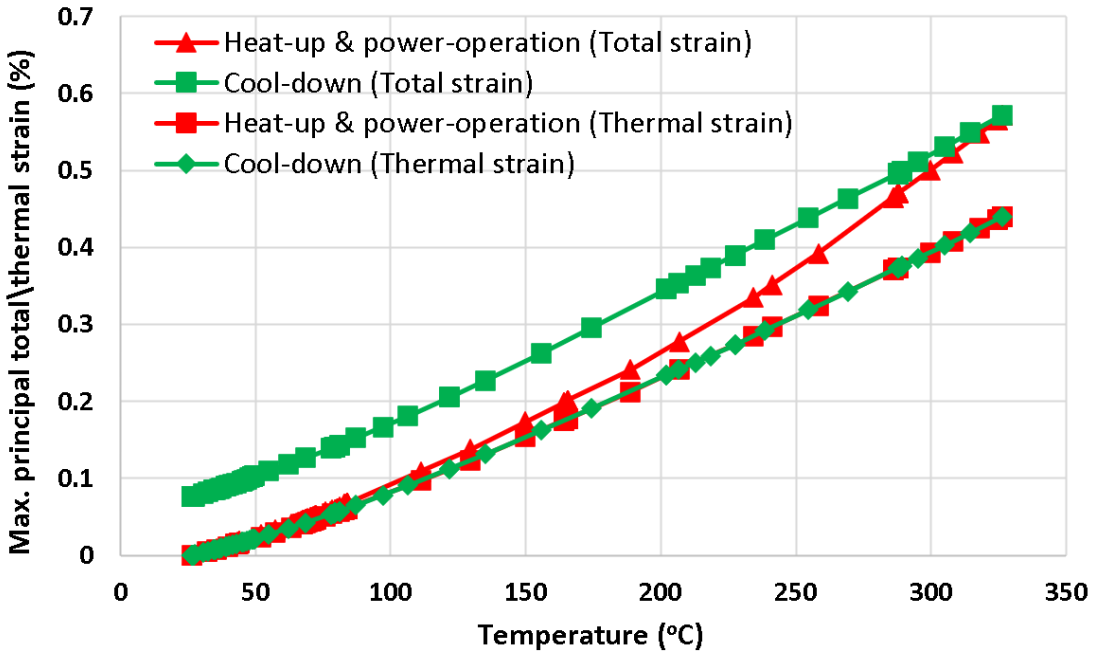

Figure 2. 29. Temperature versus maximum principal total and thermal strain at the LAS transition (between DMW and SG) region of the SG-side-nozzle of HL.

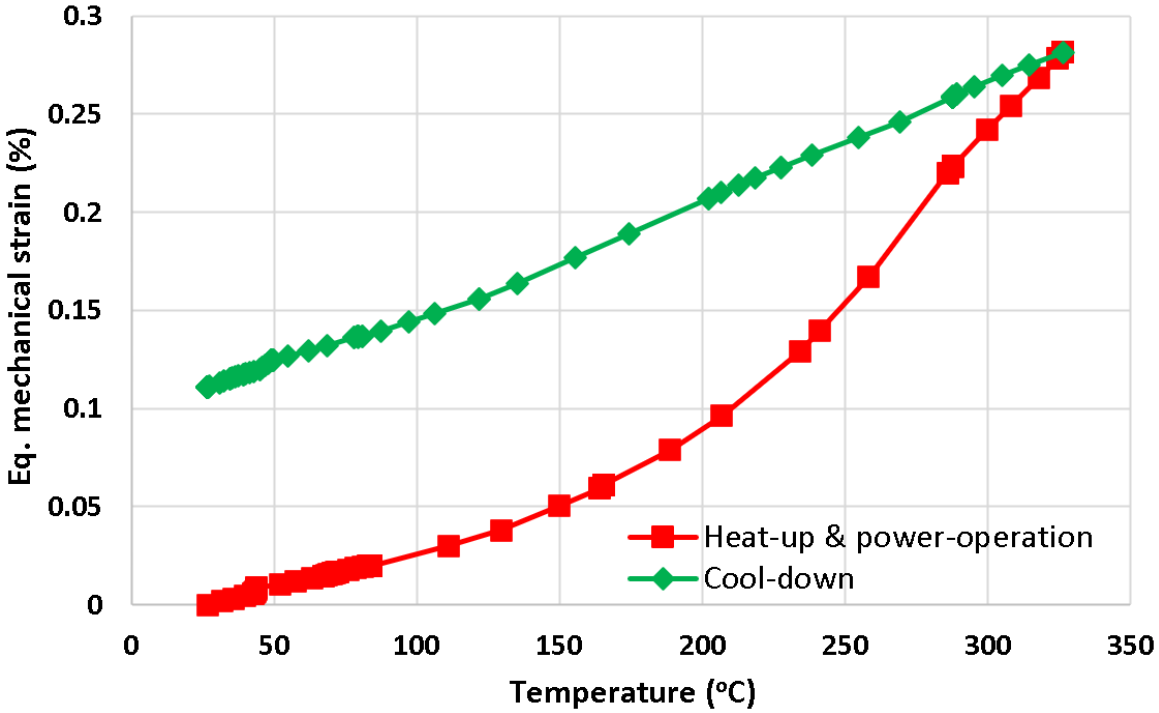

Figure 2. 30. Temperature versus multi-axial-equivalent mechanical strain at the LAS transition (between DMW and SG) region of the SG-side-nozzle of HL.

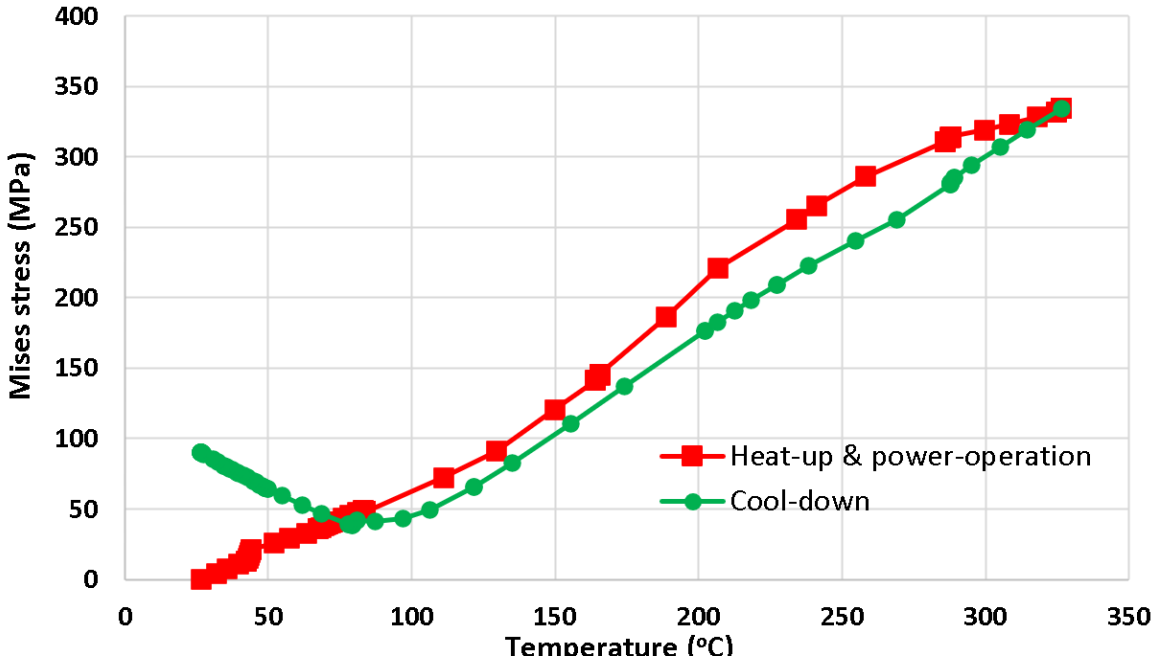

Figure 2. 31. Temperature versus multi-axial-equivalent or Von-Mises stress at the LAS transition (between DMW and SG) region of the SG-side-nozzle of HL.

Table 2. 10. Summary of various strain, stress amplitudes, and estimated of SG-side nozzle of HL.

Parameters	DMW region	⊗Non-DMW region
Max. of max. principal total strain range (%)	0.551	NA
Max. of max. principal thermal strain range (%)	0.302	NA
Max. of equivalent mechanical strain range (%)	0.239	NA
Max. of equivalent mechanical strain amplitude (%)	**0.12**	NA
Max. of von Mises stress amplitude (MPa)	368	NA
Residual equivalent mechanical strain after 1st cycle (%)	**0.014**	NA
Residual equivalent (von Mises) stress after 1st cycle (MPa)	165	NA
Mean in-air life, N_a (cycles)	>1e6	NA
Design in-air life, $N_d = \left(\frac{1}{20}\right) * N_a$ (cycles)	>1e5	NA
F_{en}	3.75	
Mean PWR water life, $N_w = \left(\frac{1}{Fen}\right) * N_a$ (cycles)	>1e6	NA
Design PWR water life, $N_{w,d} = \left(\frac{1}{Fen}\right) * N_d$ (cycles)	>1e5	NA
Best case scenario: Mean PWR water life i.e., minimum N_w of all regions (cycles)	**>1e6**	
Worst case scenario: Minimum possible PWR water life i.e., minimum $N_{w,d}$ of all regions (cycles)	**>1e5**	

2.3.6 Strain Profile of SS Base Pipe of HL and the Corresponding Fatigue Life

Figure 2.32 shows the temperature versus maximum principal total and thermal strain at the SS base pipe region of HL. The corresponding multi-axial-equivalent mechanical strain and von Mises stress profiles are shown in Figures 2.33 and 2.34, respectively. Table 2.11 shows the corresponding summary of various strain, stress amplitudes, and fatigue lives. From Figure 2.33, the HL pipe can experience significant strain amplitude of 0.51%, plastic regime, and resulting high residual strain of 0.554%. Accordingly, this can lead to the worst possible PWR-water life of 76 cycles.

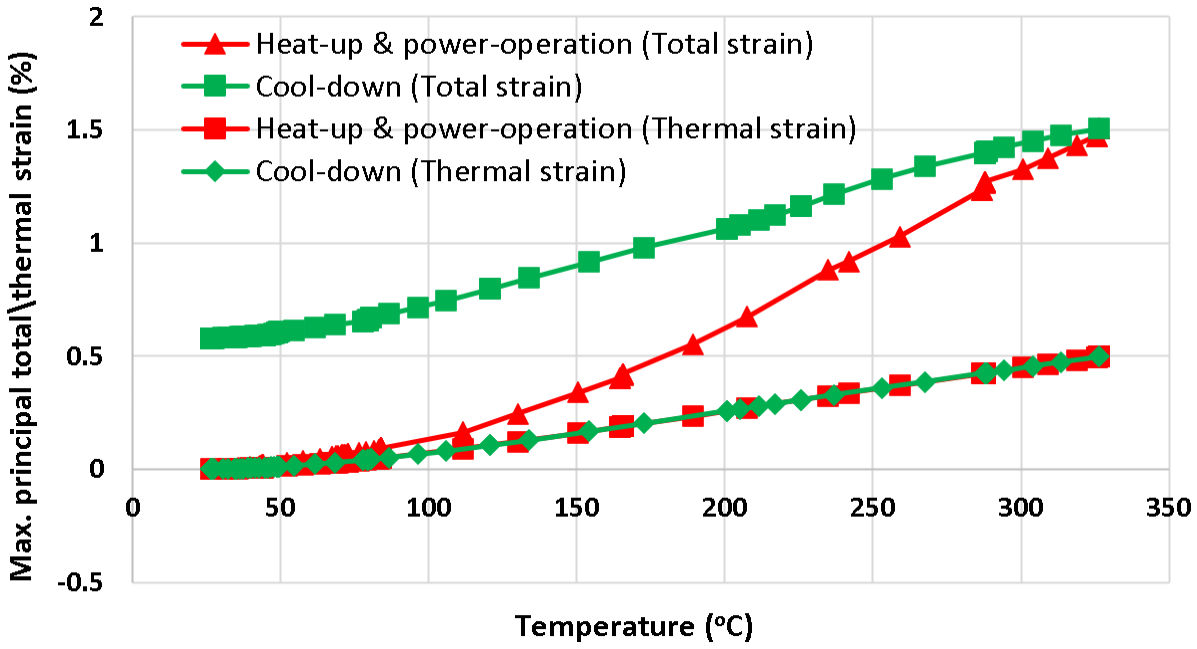

Figure 2. 32. Temperature versus maximum principal total and thermal strain at the SS base pipe region of HL.

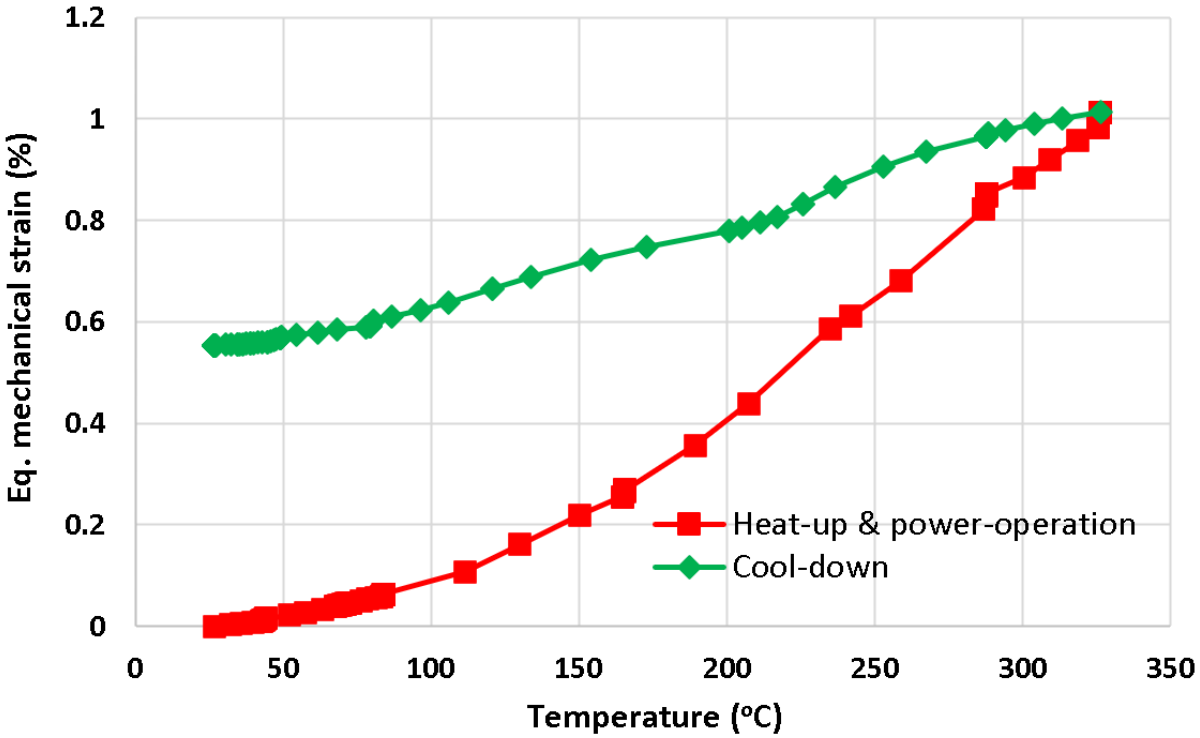

Figure 2. 33. Temperature versus multi-axial-equivalent mechanical strain at the SS base pipe region of HL.

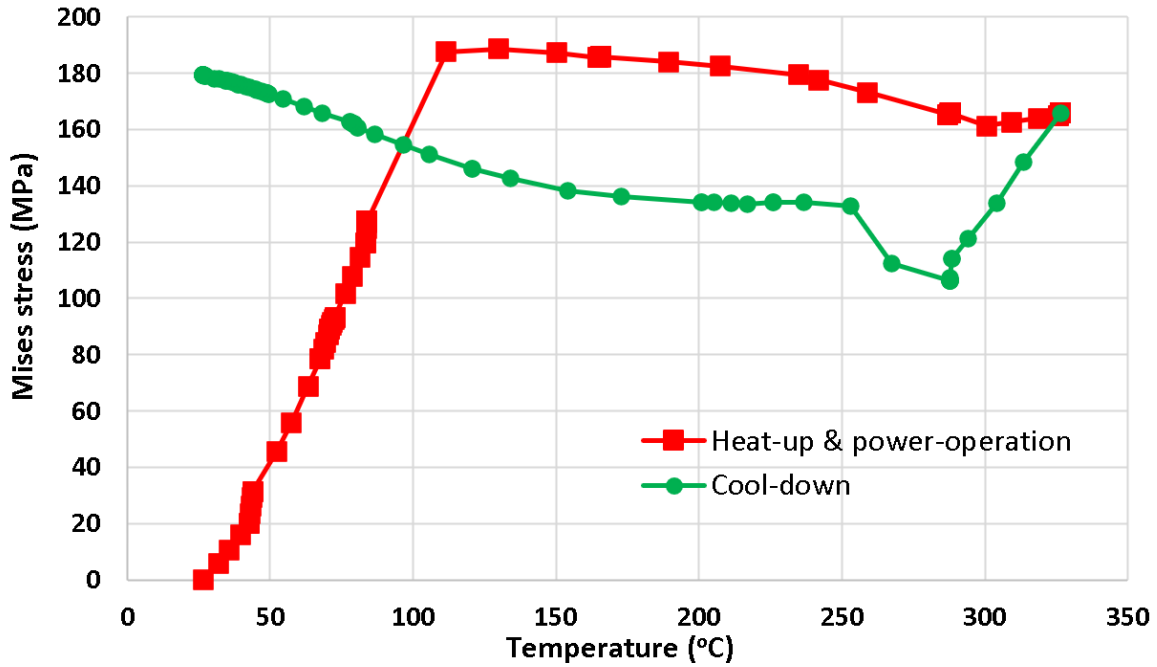

Figure 2. 34. Temperature versus multi-axial-equivalent or Von-Mises stress at the SS base pipe region of HL.

Table 2. 11. Summary of various strain, stress amplitudes, and life of SS base pipe region of HL.

Parameters	SS base pipe region of HL
Max. of max. principal total strain range (%)	1.506
Max. of max. principal thermal strain range (%)	0.498
Max. of equivalent mechanical strain range (%)	1.013
Max. of equivalent mechanical strain amplitude (%)	**0.51**
Max. of von Mises stress amplitude (MPa)	189
Residual equivalent mechanical strain after 1st cycle (%)	**0.554**
Residual equivalent (von Mises) stress after 1st cycle (MPa)	179
Mean in-air life (N_a), cycles	5712
Design in-air life ($N_d = \left(\frac{1}{20}\right) * N_a$), cycles	286
F_{en}	3.75
Mean PWR water life ($N_w = \left(\frac{1}{Fen}\right) * N_a$), cycles	1523
Design PWR water life ($N_{w,d} = \left(\frac{1}{Fen}\right) * N_d$), cycles	76
Best case scenario: Mean PWR water life (minimum N_w of all regions), cycles	**1523**
Worst case scenario: Minimum possible PWR water life (minimum $N_{w,d}$ of all regions), cycles	**76**

2.3.7 Imaginary Temperature versus Strain Profile had the Cycling Continued

The above temperature versus strain profiles is based on a single-cycle FE model. If multi-cycle FE results were available, the corresponding strain profile could evolve with respect to time or fatigue or fuel cycles. This can be in either increasing direction or with a stagnant strain condition. This is similar to creep deformation when the strain is not being controlled (as in case of a conventional uniaxial strain-controlled fatigue test). In actual field conditions, the deformation (or strain) is the effect, whereas the associated causes are the field variables such as temperature, pressure, coolant environment and irradiation. Figure 2.35 shows the schematic of time evolving temperature versus strain profiles (when strains are not being controlled). Nevertheless, the actual behavior of the reactor component (under multiaxial loading as well as under the above-mentioned field variables) is hard to repeat through a simplistic laboratory experiment (primarily based on uniaxial strain-controlled fatigue tests). To ascertain the behavior of realistic strain growth in a reactor component, more advanced modeling (such as through the combined use of physics-based FE models and AI-ML-based data-driven models, etc.) and experimental characterization are required.

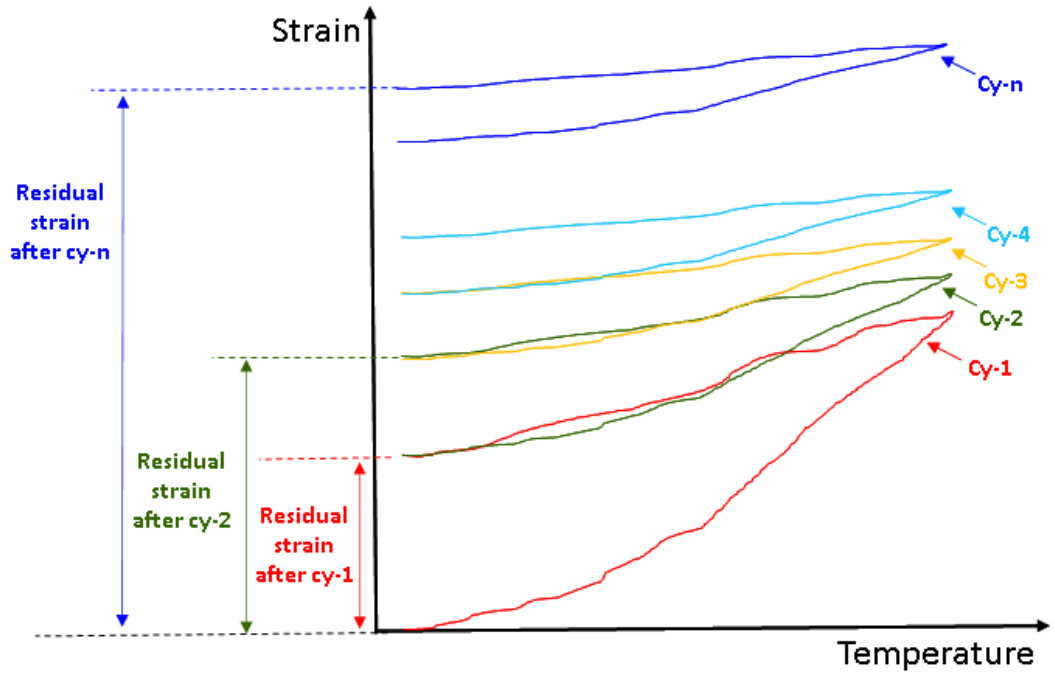

Figure 2. 35. Schematic of time evolving temperature versus strain profiles (when strains are not being controlled).

3 Preliminary Development of SQL-based Database and Python-based Application Programming Interface

Material test-based data alone can't predict the complex system-level loading train. Although a system-level FE model can predict a multi-axial loading train, even that is not sufficient to predict the behavior of a component subjected to dynamically changing temperature-pressure transients. We are developing AI-ML-based interconnected applications (apps) that can feed into each other to eventually predict the life of a safety-critical component in real time given a real-time plant process measurement. Figure 3.1 shows the schematic of AI-ML-based data-driven DT framework showing different physics apps and dataflow directions. Structural parameters that affect the life of a component (e.g., strain, stress, etc.) are geometry-dependent and localized. For this reason, sensor data (e.g., such as virtual sensor data from an FE model) are required at thousands to millions of locations for training an AI-ML based data-driven model. These virtual sensor data along with real-sensor data (e.g., both historical and current process measurements) need to be stored in an appropriate industry-standard database for realistic industrial use of the DT model. At the same time, the database must be interfaced with the various constituent predictive models or applications. Towards the overall goal of developing an AI-ML- based data driven framework that can run in real time without depending on a conventional FE model for each changing and time-dependent process conditions, we built a preliminary SQL- based database. We will improve this database as the work continues. Additionally, we developed a preliminary python-based application programming interface (API) to interact with the database and different data-driven physics-infused applications (some of which are already developed [5] or need to be developed). For example, Figure 3.2 shows the screenshot of the database based on industry standard MySQL platform. Whereas Figure 3.3 shows the example reading of the temperature data (from the MySQL database and using the developed API) at a typical 3D location of the HL nozzle.

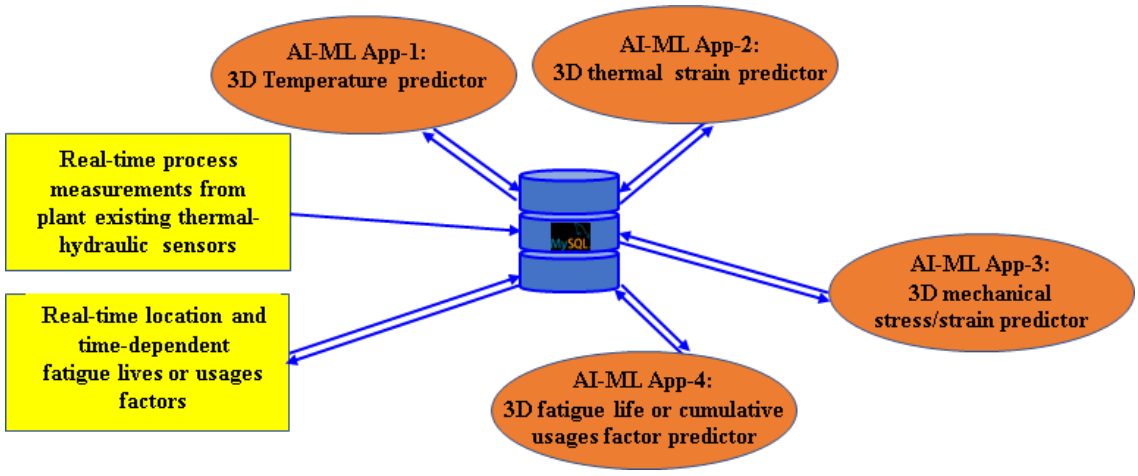

Figure 3. 1. Schematic of AI-ML based data-driven DT framework showing different physics apps and dataflow directions.

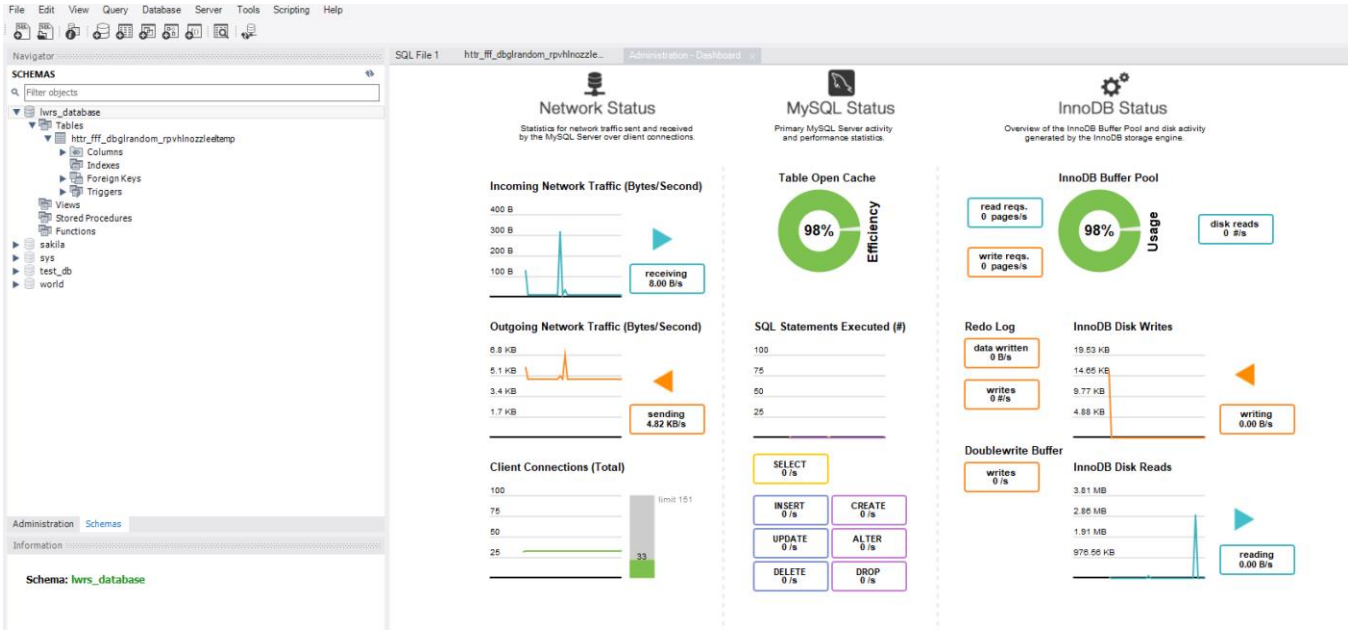

Figure 3. 2. Screenshot of the architected database based on industry standard MySQL platform.

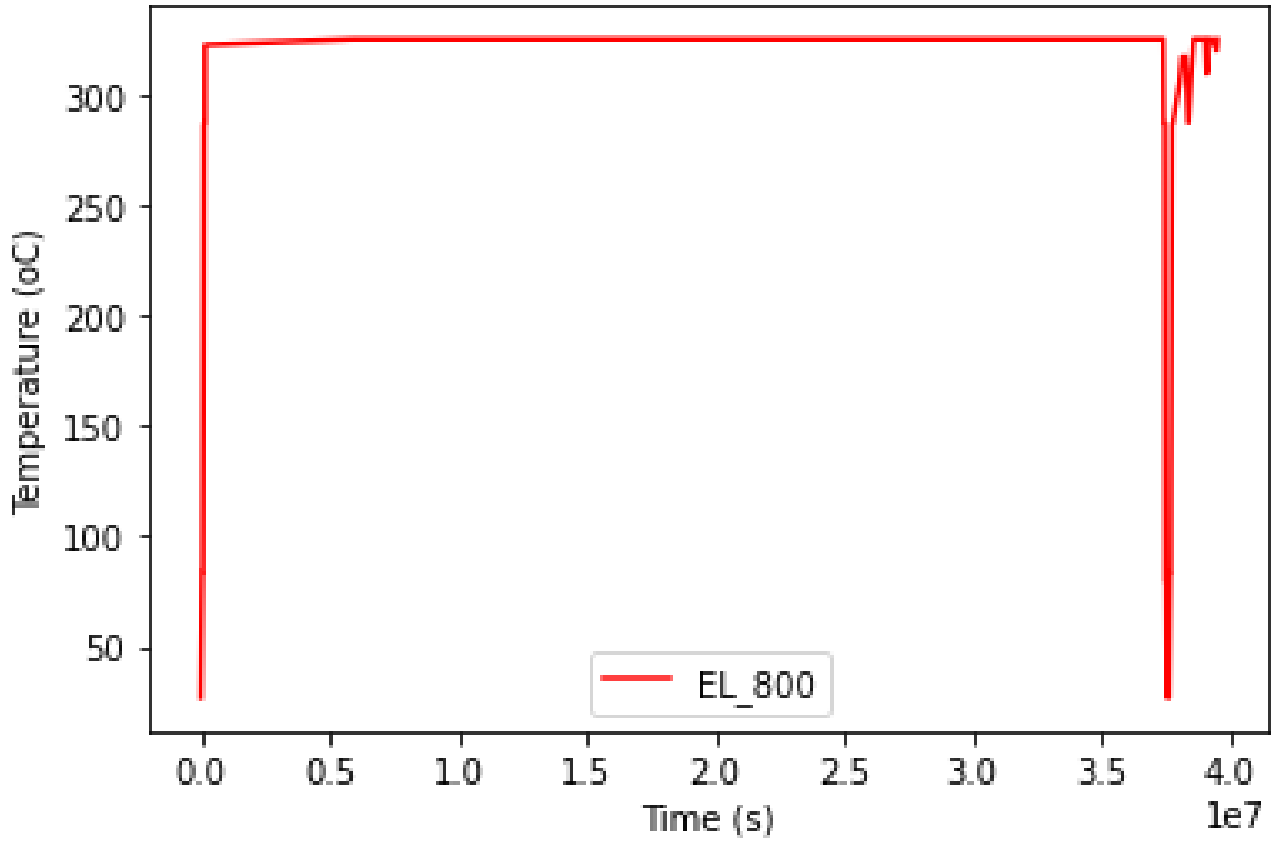

Figure 3. 3. Example reading of the temperature data (from the architected MySQL database and using the developed API) at a typical 3D location of the HL nozzle.

4 Algorithm Development for Predicting Time- and Location- Dependent Cumulative Usage Factor or Fatigue Lives

We developed a preliminary distributed-strain-transient-based cumulative usage factor estimation model and present the related results in this section. The related software or algorithms were developed towards the life-estimation leg (or applications) of the overall DT framework. We assumed that, given the real-time process measurements (from few existing thermal-hydraulic or plant process measurement sensors), the DT framework would be able to predict the distributed mechanical strain at random locations (inside/outside thickness of a component) and in real time. Based on the resulting time and location-dependent strain, the corresponding lives or cumulative usage factor (CUF) can be estimated. Although, the time and location dependent strain profiles to be passed from a strain predictor application or leg of the overall DT framework (which is yet to be fully developed), the presented results (CUF under PWR water environment: CUF_{en}) are simulated based on synthetic strain profiles which are artificially simulated at 57 locations along the length of a PWR surge line. Two cases were simulated with a maximum strain range of a) 1.672% (to compare with the related single-location-based life estimation results presented in section 2) and b) 1.2% (to compare the results with experimental results reported in NUREG-6909, Rev-1 [2] for an equivalent strain amplitude of 0.6%). The synthetic strain profiles were generated at some example 3D locations of a PWR surge line as highlighted in Figure 4.1. These strain profiles were generated as a function of the earlier FE-simulated [5] temperature data (at those selected 3D locations) and by randomizing the profiles (during full power operations) with a maximum strain range of 1.672 % or 1.2 %.

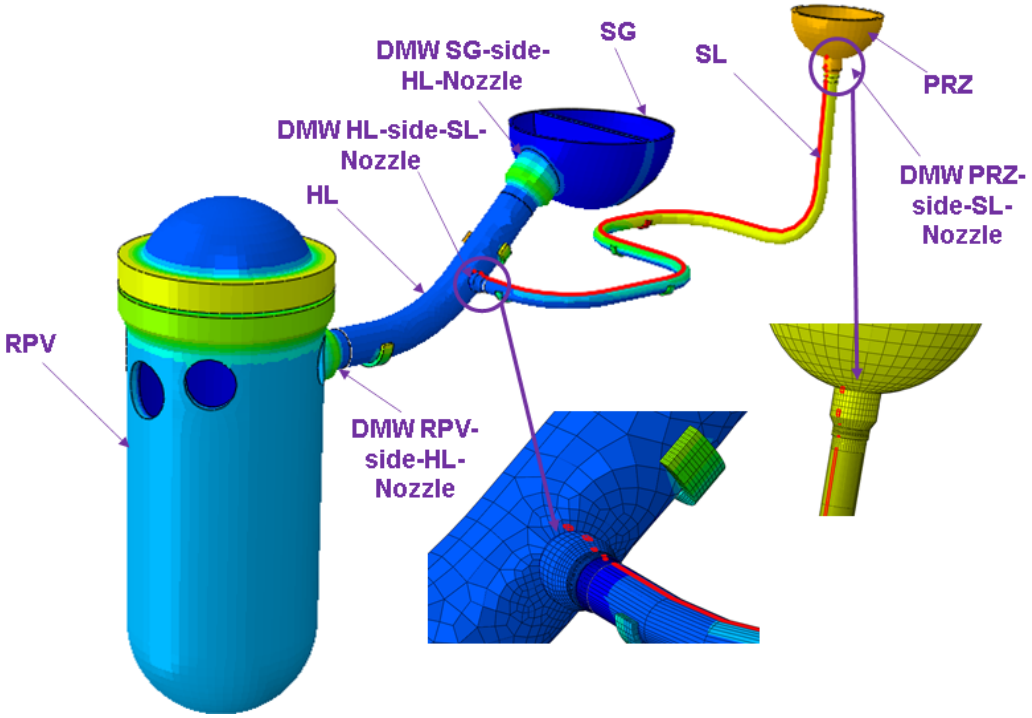

Figure 4. 1. Highlighted 53 FE element locations in red (along the OD length of SL-pipe-nozzle-assembly) at which the temperatures were predicted [5].

4.1 Case-a: Strain Range of 1.672%

We estimated the location- and time-dependent cumulative usage factors based on location- and time-dependent strain profiles with a maximum strain range of 1.672%. For example, Figure 4.2 shows the time versus synthetic strain-range profiles at 53 3D random locations along the length of SL (refer to Figure 4.1). This is with the assumption of 100 fuel cycles each with 1.1912 years. Figure 4.3 shows a magnified version of Figure 4.2, whereas Figure 4.4 shows the corresponding time versus maximum strain amplitudes. For all the locations (refer to Figure 4.1), a fixed F_{en} value of 3.75 was considered, which is the same as all the life results presented in Section 2. We discuss the reason for selecting a fixed F_{en} in Section 2. Additionally, the F_{en} value of 3.75 is reasonable based on our earlier work [10]. For example, Figure 4.5 shows the possible F_{en} values and associated confidence bands for a given strain amplitude. Figure 4.6 shows the time versus estimated CUF_{en} for the strain-range profiles shown in Figure 4.2 and considering a design-curve correction factor of 12. Figure 4.7 shows the magnified version of Figure 4.6 whereas Figure 4.8 shows the time versus estimated CUF_{en} for the strain-range profiles shown in Figure 4.2 and considering a design-curve correction factor of 20. Figure 4.9 shows the magnified version of Figure 4.8. The above two sets of results show that the CUF can vary depending on locations. Nevertheless, the algorithm and the related software can automatically predict the given strain information which depends on time and location. To determine how the algorithm results compare (repeatable or not) with respect to single location-based prediction results as presented in Section 2, we ran the same code but assuming same strain profiles (with a maximum strain range of 1.672% and considering a design-curve correction factor of 20) at all the 53 locations. Figure 4.10 shows the related results. From this figure at a fatigue life of 25 cycles the approximate CUF_{en} is 1. This is very close to the life result estimated at the highest strain location of SL (i.e., at HL-side nozzle of SL, refer to Table 2.6).

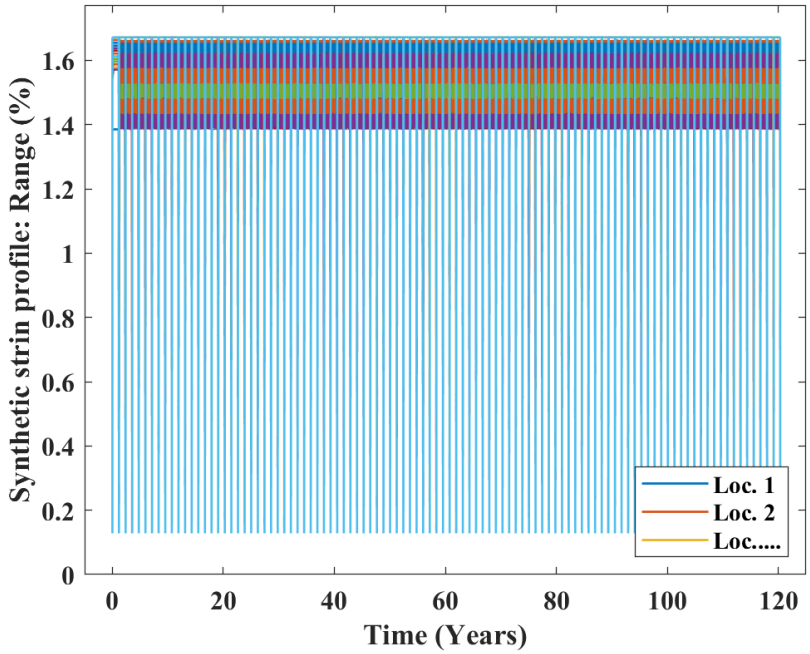

Figure 4. 2. Time versus synthetic strain (range) profiles at 53 3D random locations along the length of SL (refer to Figure 4.1), with assumption of 100 fuel cycles (each with 1.1912 years) and a maximum strain range of 1.672%.

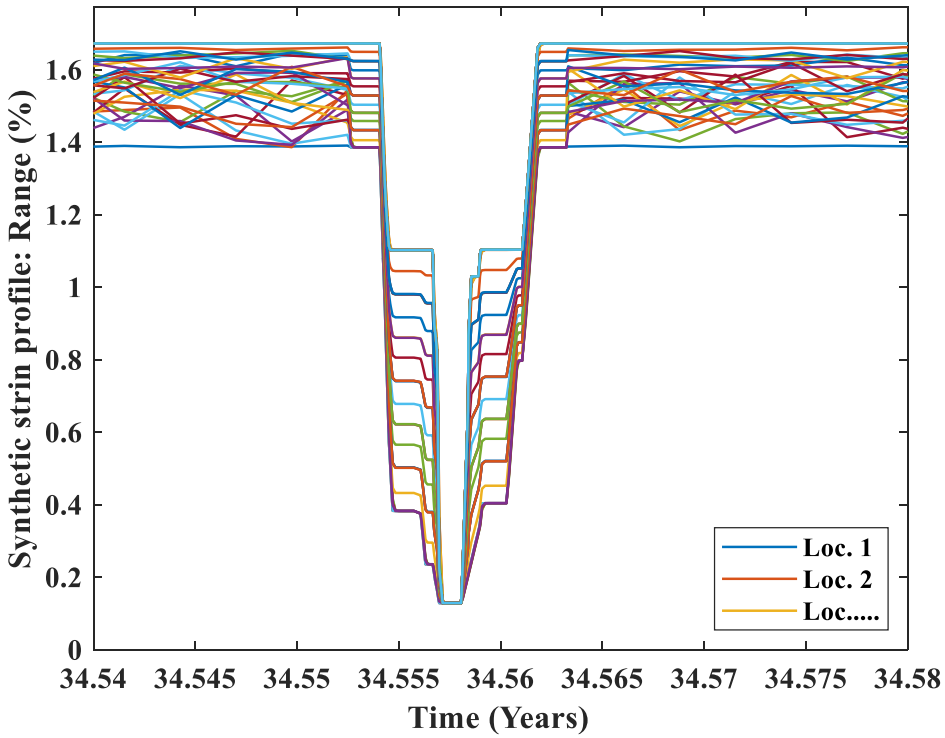

Figure 4. 3 Magnified version of Figure 4.2.

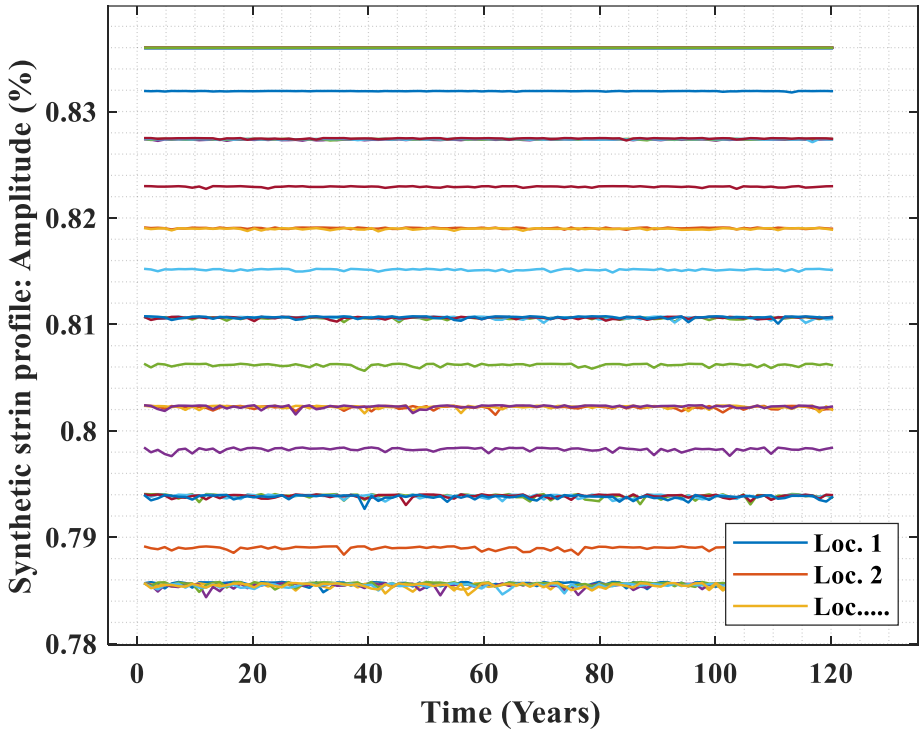

Figure 4. 4. Time versus maximum strain amplitudes (of the strain-range profiles shown in Figure 4.2) at 53 3D random locations along the length of SL (refer to Figure 4.1).

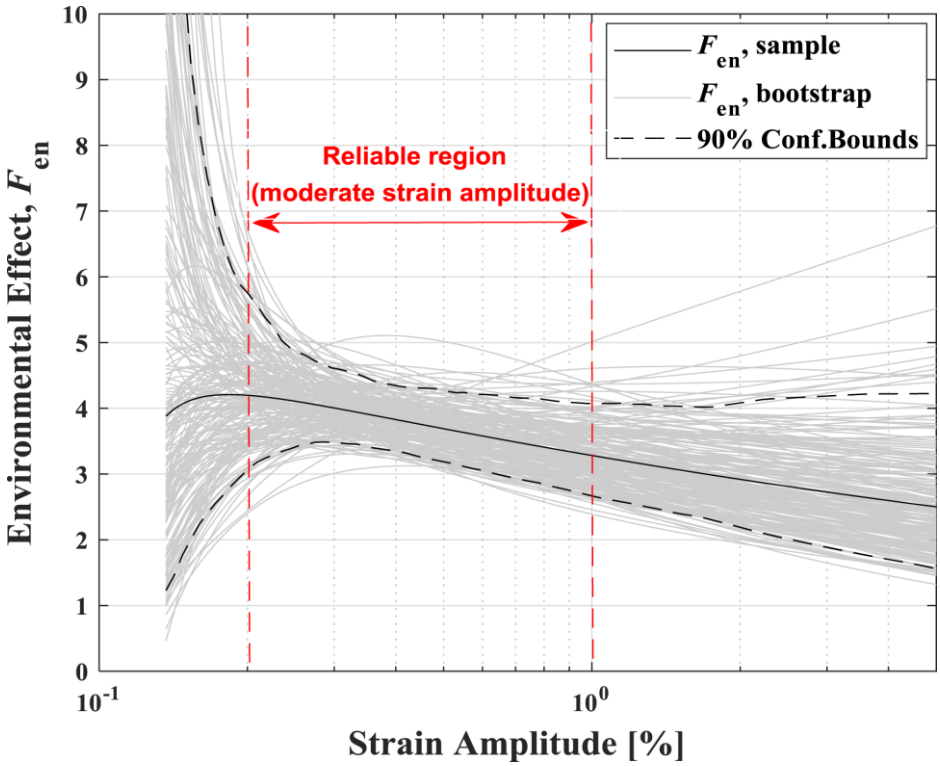

Figure 4. 5. Possible Fen values and associated confidence bands for a given strain amplitude (refer to our earlier work [10])

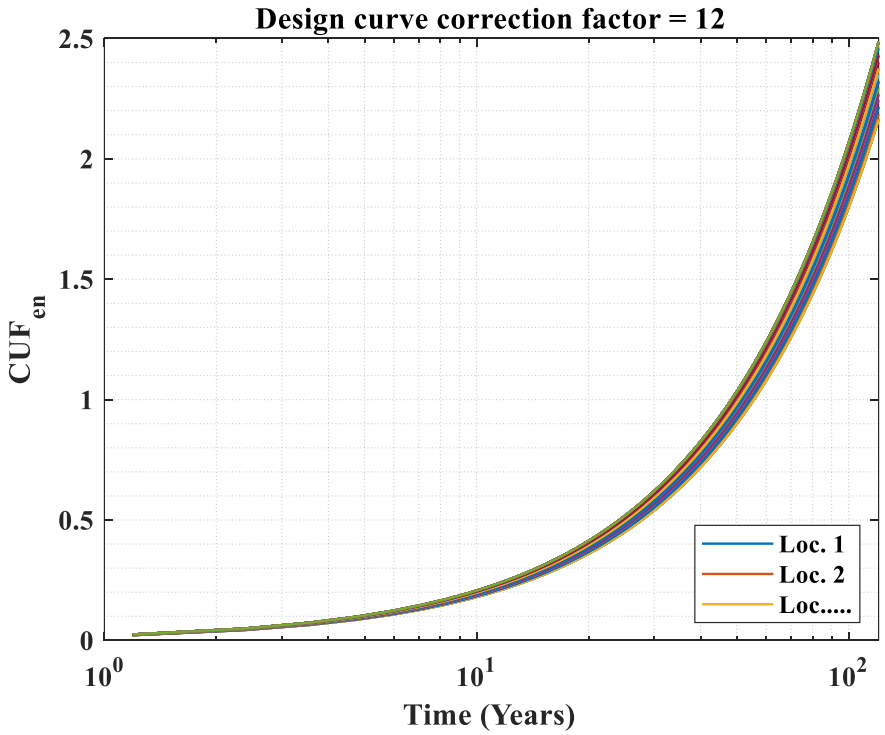

Figure 4. 6. Time versus estimated CUF_{en} (for the strain-range profiles shown in Figure 4.2 and considering a design-curve correction factor of 12) at 53 3D random locations along the length of SL (refer to Figure 4.1).

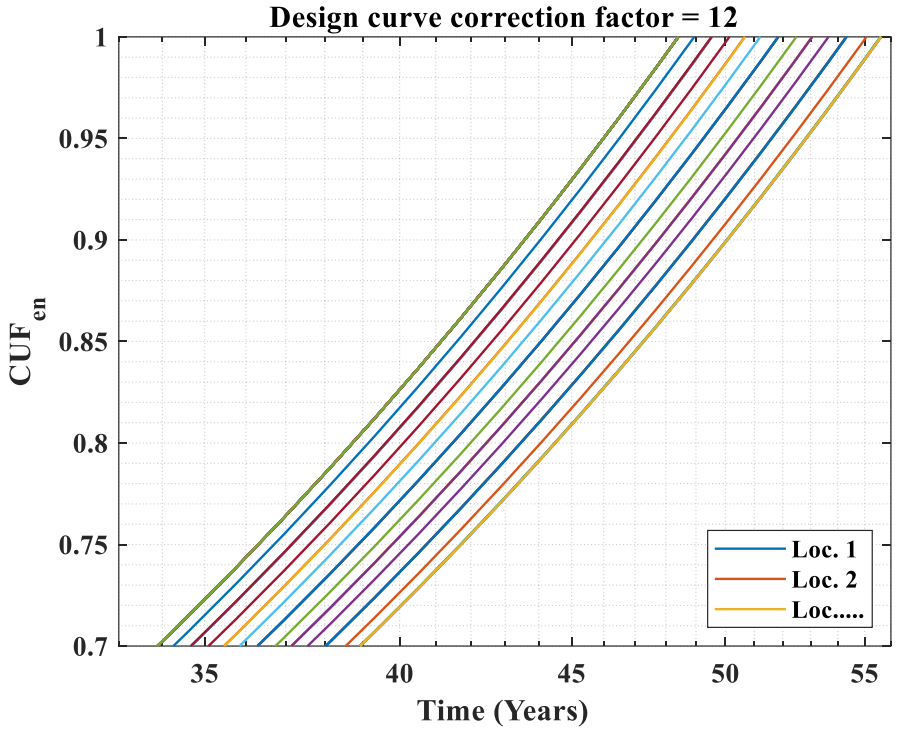

Figure 4. 7 Magnified version of Figure 4.6.

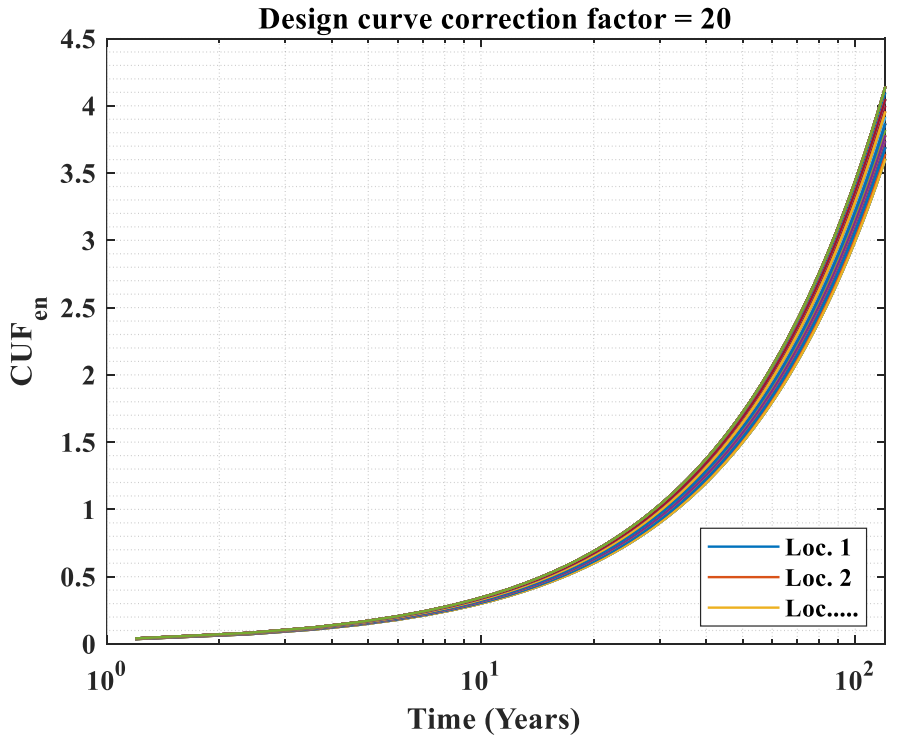

Figure 4. 8. Time versus estimated CUF_{en} (for the strain-range profiles shown in Figure 4.2 and considering a design-curve correction factor of 20) at 53 3D random locations (refer to Figure 4.1) along the length of SL.

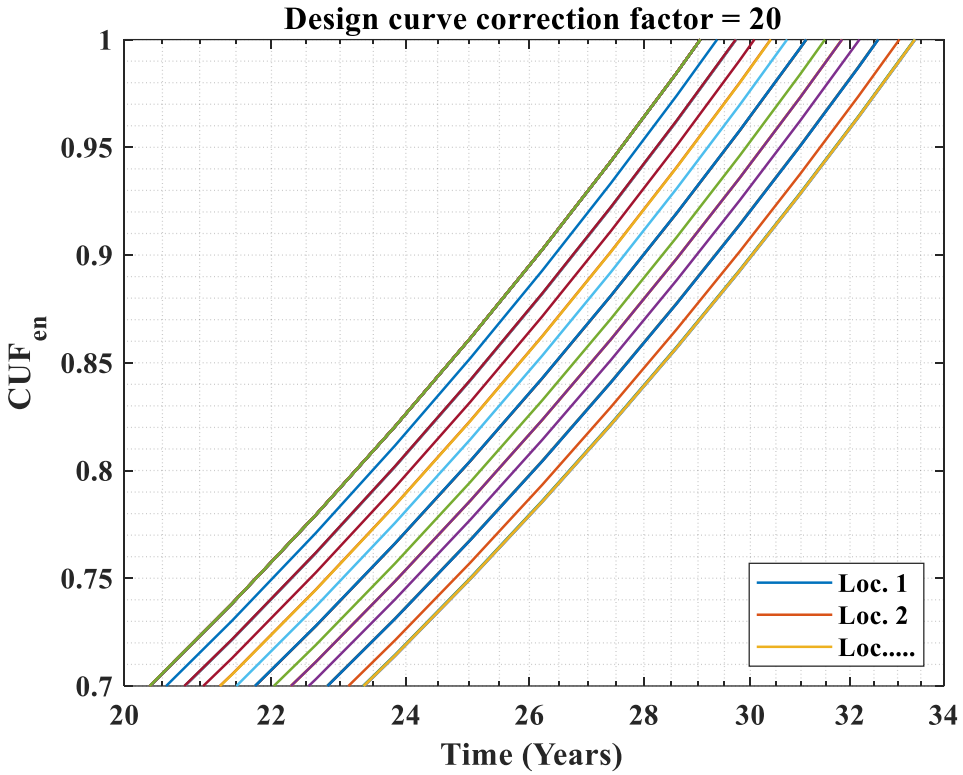

Figure 4. 9 Magnified version of Figure 4.8.

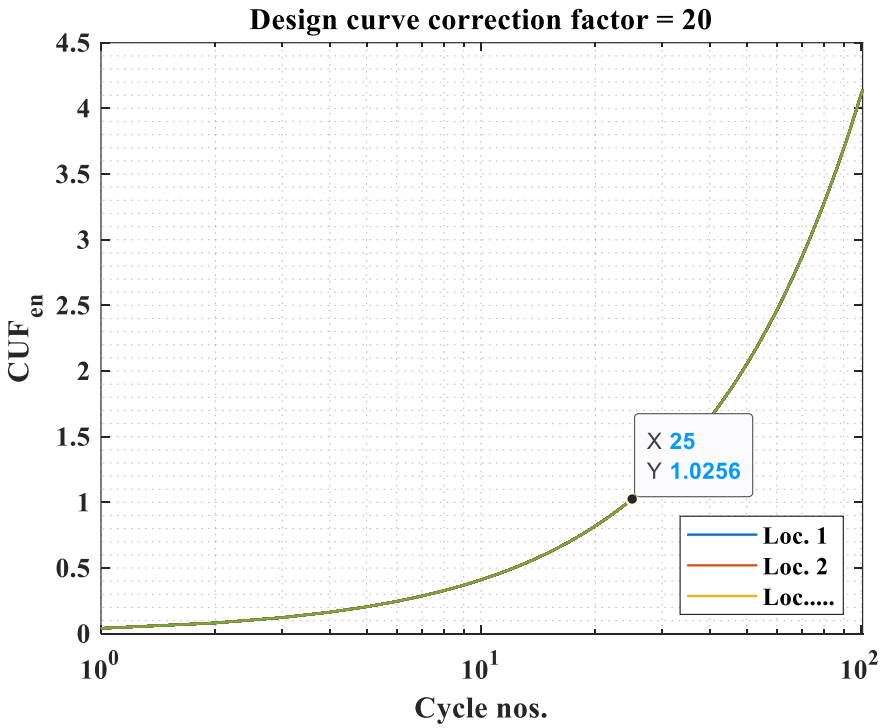

Figure 4. 10. Time versus estimated CUF_{en} with assumption of a fixed strain profile (at all the 53 3D locations along the length of SL, refer to Figure 4.1) and considering a maximum strain range of 1.672 % and a design-curve correction factor of 20.

4.2 Case-b: Strain Range of 1.2 %

We estimated the location-and-time-dependent cumulative usage factors based on location-and-time-dependent synthetic strain profiles with a maximum strain range of 1.2%. We will use this estimate for comparison with experimental results reported in NUREG-6909, Rev-1 [2] for an equivalent strain amplitude of 0.6%. As with the previous case, we assumed a fixed F_{en} value of 3.75 for all the locations. Figure 4.11 shows the synthetic strain (range) profiles at 53 3D random locations along the length of the SL (refer to Figure 4.1) for which we predicted the location-dependent CUFs. Figure 4.12 shows the magnified version of Figure 4.11, whereas Figure 4.13 shows the corresponding time versus maximum strain amplitudes. Figure 4.14 shows the corresponding location-dependent CUF_{en} with consideration of a design-curve correction factor of 12. Figure 4.15 shows the magnified version of Figure 4.14, whereas Figure 4.16 shows the location-dependent CUFs for the strain-range profiles shown in Figure 4.11 and considering a design-curve correction factor of 20. Figure 4.17 shows the magnified version of Figure 4.16. Figure 4.15 shows that the simulated maximum life with design curve factor of 12 is approximately 101 cycles (or the equivalent of 101*1.1912 = 120 years) at an approximate CUF of 1. Hence the equivalent approximate experimental life in air would be 101*12 = 1212 cycles. Similarly, from Figure 4.17 the simulated maximum life with design curve factor of 20 is approximately 60 cycles (or the equivalent of 60*1.1912 = 71.5 years). This is at an approximate CUF of 1. Hence the equivalent approximate experimental life in air would be 60*20 = 1200 cycles. For both cases (design curve factor of 12 and 20) the estimated equivalent experimental life is approximately 1200 cycles. Actual experimental data of austenitic SS (Figure 4.18 in this report or Figure 4-39 in NUREG-6909, Rev-1 [2]) demonstrates that at 0.6% strain amplitude, the approximate experimental lives vary from 80 cycles (at strain rate of 0.00001 %/s) to 2000 cycles (at strain rate of 0.4 %/s). Hence the estimated equivalent experimental life (based on the discussed predictive model results) of approximately 1200 cycles is well within the range of an actual experimental life of 80 to 2000 cycles (at a strain amplitude of 0.6 %). Nevertheless, the aim of this work to develop and test the related physics, algorithm, and software. The developed methodology can eventually be implemented into the overall DT framework (depicted in Figure 3.1). The actual strain profile must be fed from the mechanical strain predictor leg of the DT framework rather than the synthetic or assumed strain profiles (as used in the presented results). Accordingly, the location-dependent CUFs can be different than the CUF results presented in this report. The overall DT framework is under development.

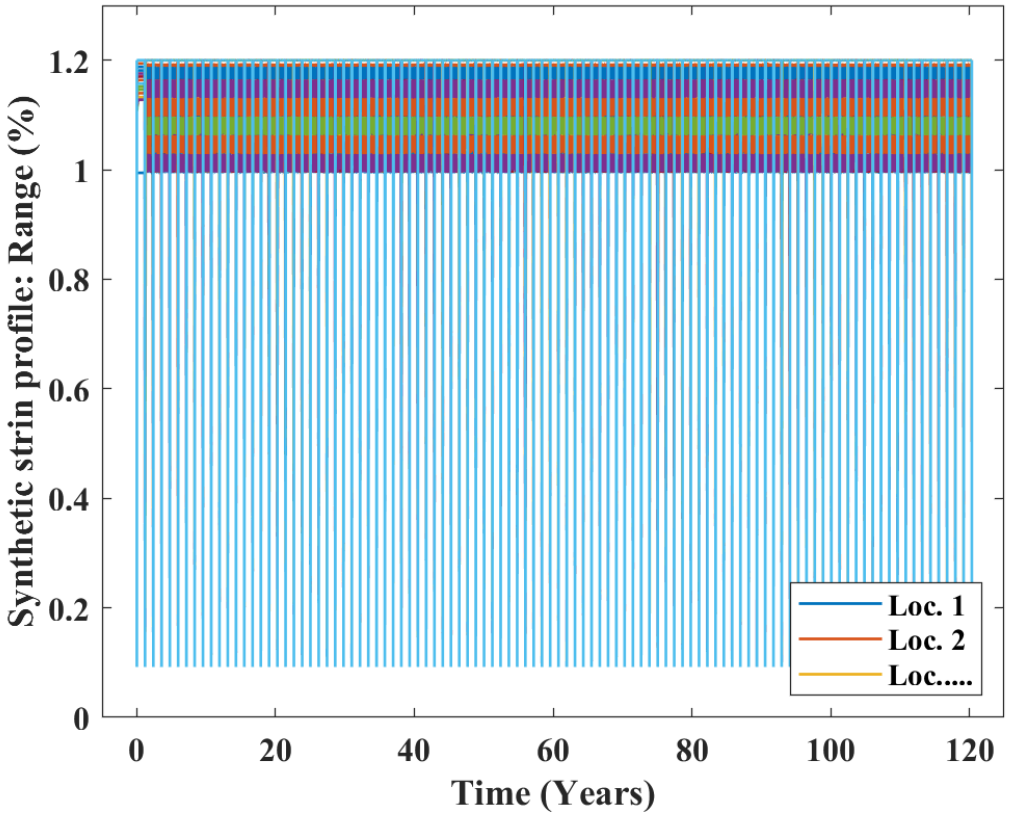

Figure 4. 11. Time versus synthetic strain (range) profiles at 53 3D random locations along the length of SL (refer to Figure 4.1), with assumption of 100 fuel cycles (each with 1.1912 years) and a maximum strain range of 1.2 %.

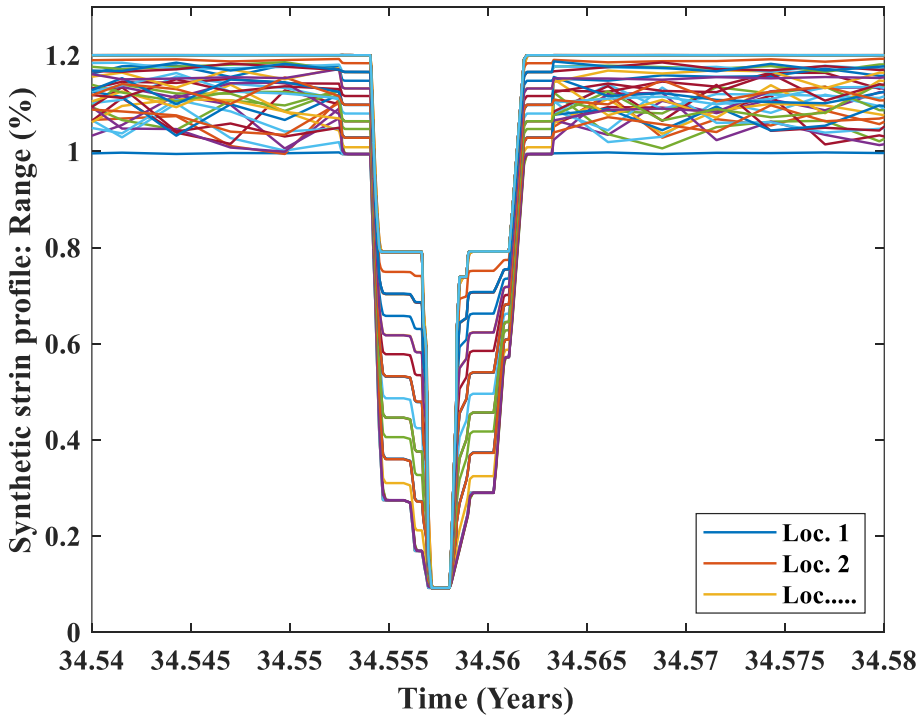

Figure 4. 12 Magnified version of Figure 4.11.

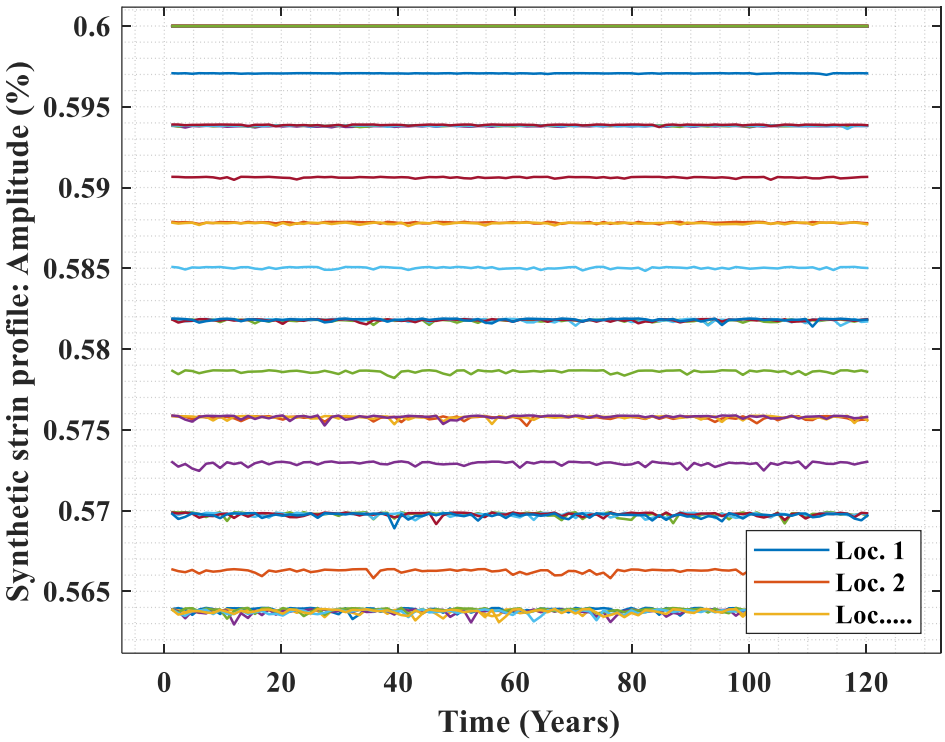

Figure 4. 13. Time versus maximum strain amplitudes (of the strain-range profiles shown in Figure 4.11) at 53 3D random locations along the length of SL (refer to Figure 4.1).

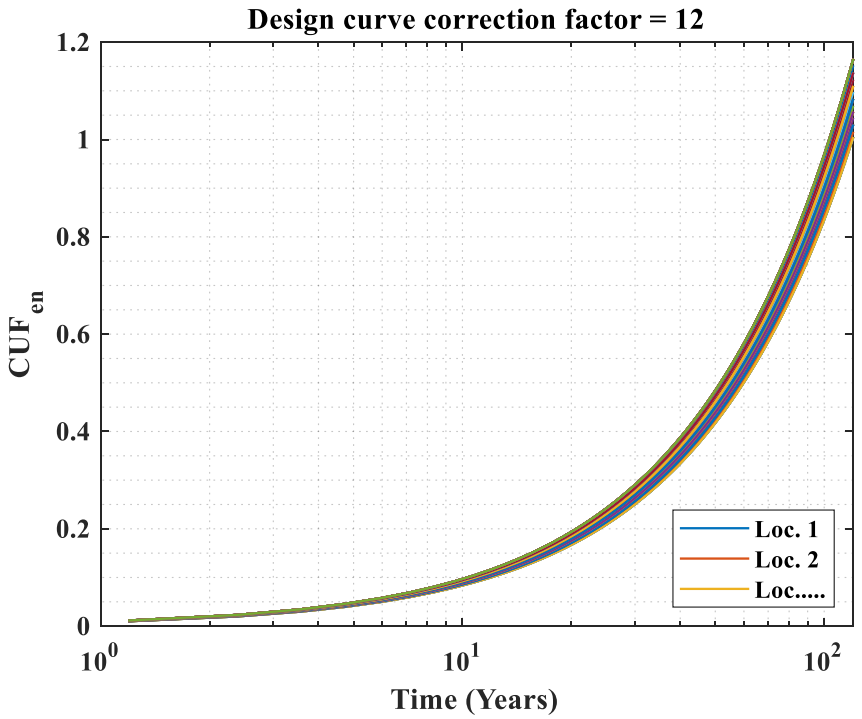

Figure 4. 14. Time versus estimated CUF_{en} (for the strain-range profiles shown in Figure 4.11 and considering a design-curve correction factor of 12) at 53 3D random locations along the length of SL (refer to Figure 4.1).

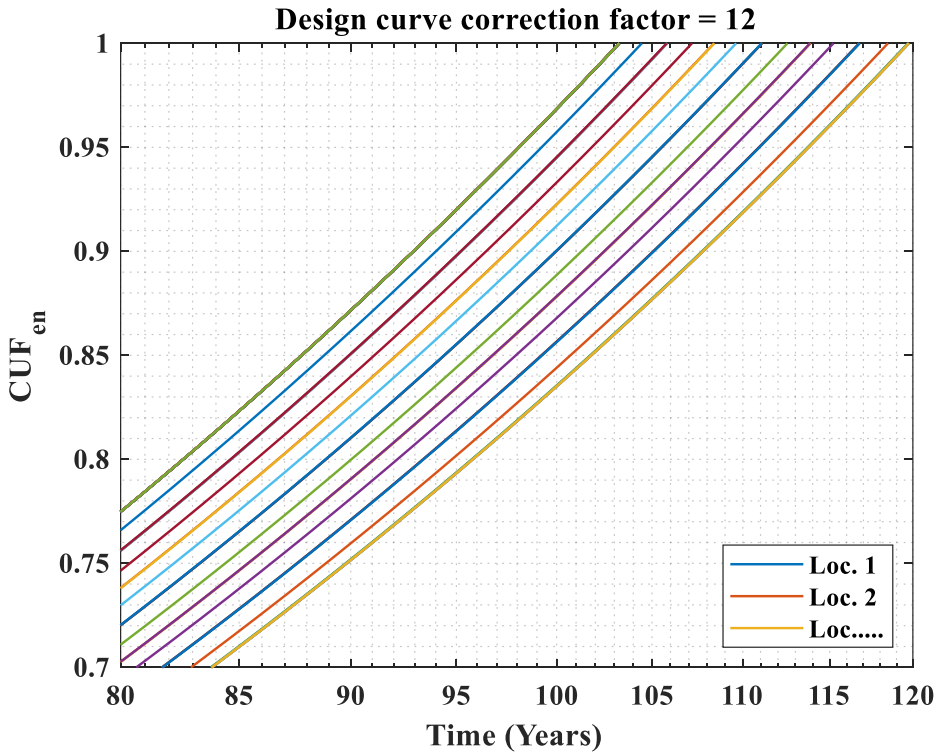

Figure 4. 15. Magnified version of Figure 4.14.

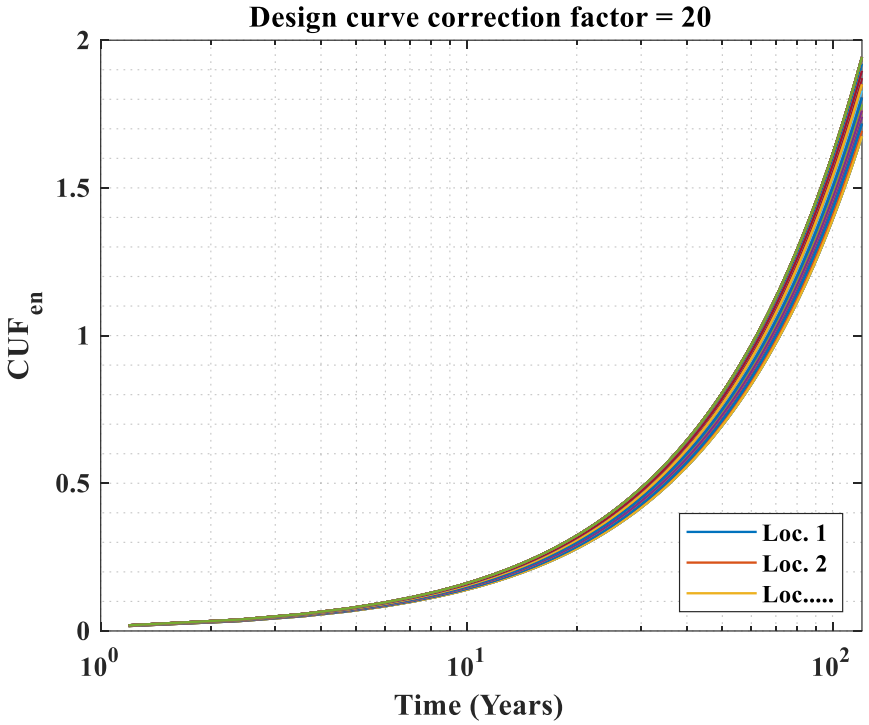

Figure 4. 16. Time versus estimated CUF_{en} (for the strain-range profiles shown in Figure 4.11 and considering a design-curve correction factor of 20) at 53 3D random locations (refer to Figure 4.1) along the length of SL.

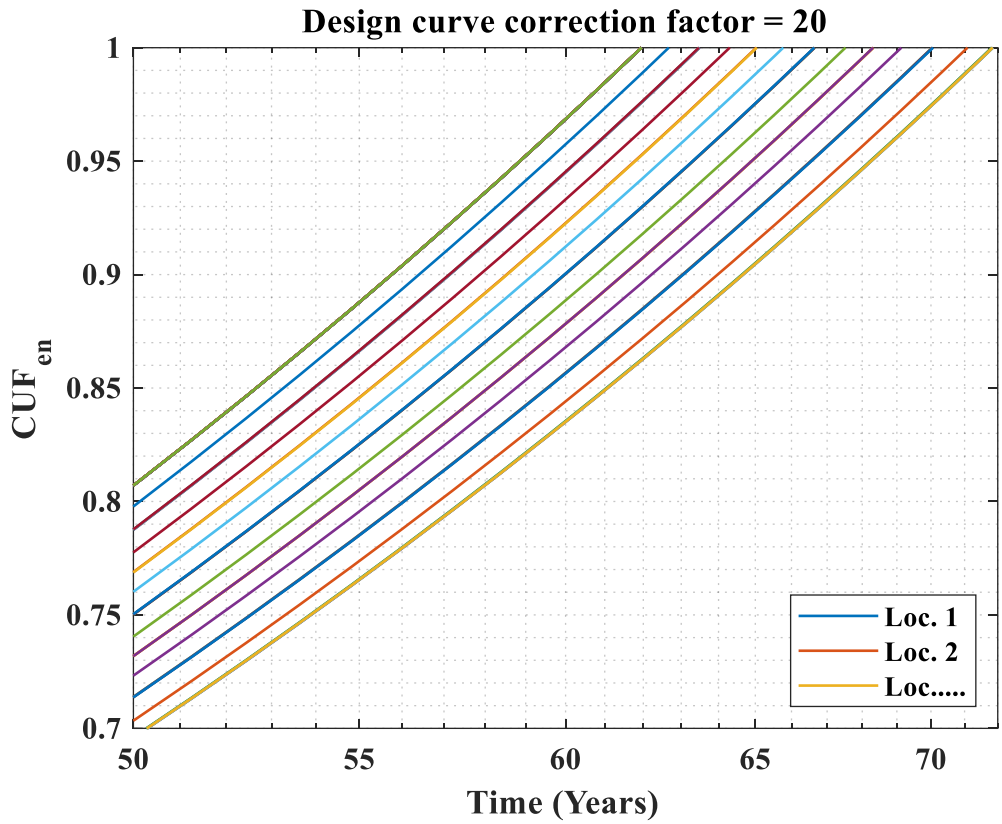

Figure 4. 17. Magnified version of Figure 4.16.

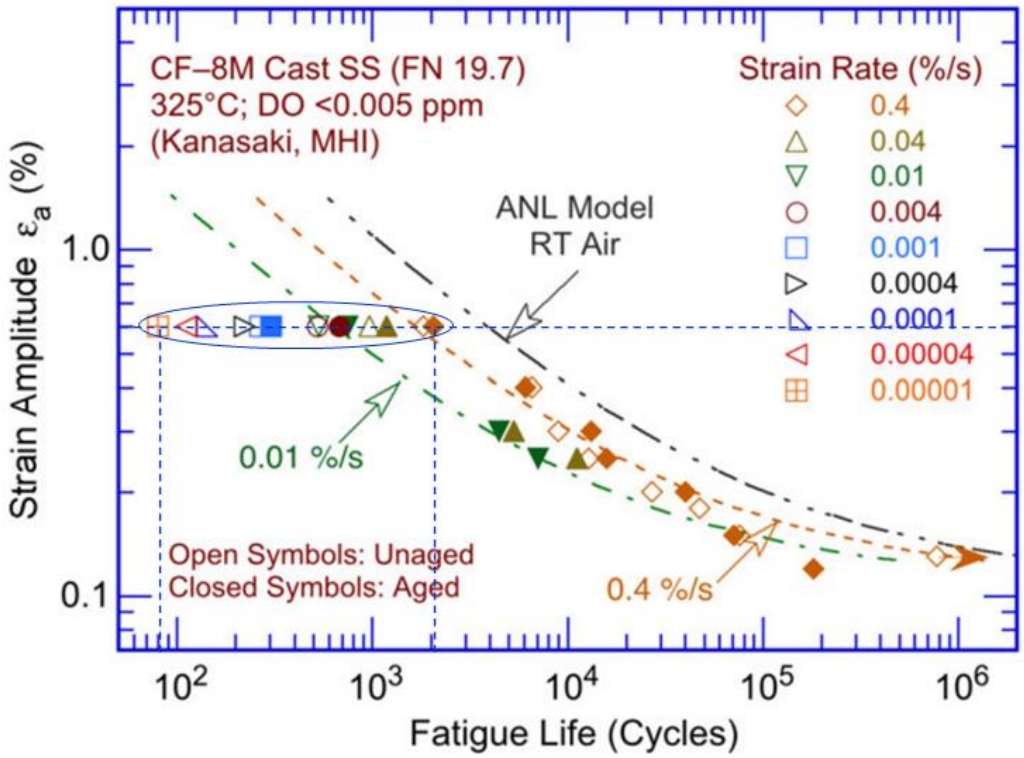

Figure 4. 18. NUREG-6909, Rev-1 [2] based experimental data.

5 Summary & Future Work

5.1 Summary

A summary of the reported work follows:

a. A system-level FE model was developed to simulate the thermal and mechanical strain profiles and associated fatigue lives of a PWR HL, SL, and their DMW-SMW nozzles under connected system thermal-mechanical boundary conditions. The results show some of the RCS components can have significantly less fatigue life compared to the other components of the RCS with similar geometry and material. Based on these results, we can surmise that the HL-side nozzle of the SL can be an issue, particularly for long-term operation of nuclear reactors. Although the reported results are geometry-specific and qualitative, since most of the NPP has a very similar configuration we can expect similar qualitative results. Nevertheless, the reported results are representative and can be used as a guideline to focus NDE-related inspection for a specific region of the RCS rather than the entire RCS. Requiring frequent and detailed NDE inspection can negatively impact the financial stability of the U.S. operating nuclear fleet. This approach can help to identify and prioritize the NDE inspections, reducing operational and maintenance costs.

b. A MySQL based database is built to store the underlying actual sensor and virtual sensor data. A python-based API was developed to interact with the database. The database will be eventually linked to the different physics legs (AI-ML-based applications) of the overall DT framework via the developed API.

c. A physics-infused software framework was developed to predict the time- and location- dependent cumulative usage factors. The underlying algorithms were tested for synthetic time- and location-dependent strain profiles.

5.2 Possible Future Works

Some of the future work in context of DT method, related algorithm and software development can be of:

a. Developing the AI-ML applications for rest of the physics replicas (such as for real time predictions of 3D thermal strain, mechanical strain, etc.) and linking to the developed database and other applications. Note, our earlier work [5] presents the AI-ML models those can be used for predicting 3D temperature at inside/outside thickness of a component given the process measurements. Similar AI-ML model development is required for predicting the thermal and mechanical strain and linking those to the life prediction model (discussed in section 4 of this report).

b. Developing the software orchestration tools for the above developed apps to make the developed framework work synchronously and in real time without any trouble.

c. CPU-GPU accelerated DT framework for handling large scale real time computing such as for real-time damage predictions at thousands to millions of 3D geometry-dependent locations or point clouds.

d. Optimized computational algorithm development as the plant operator will not have access to large scale in-premise and/or cloud based high-performance computing infrastructure for performing computationally intensive geometry and time dependent predictions.

Additionally, some of the future works in context of experimental aspects can be:

a. Fatigue testing of base (primarily on 316 SS) and both dissimilar-metal-weld (DMW) homogeneous weld and multi-metal joint specimens under component specific strain profiles (e.g., as based on the strain amplitudes reported in section 2 and following similar loading profiles reported in section 4). This is contrary to the conventional fatigue testing with typical R = -1 type loading with a typical strain amplitude of 0.5%.

b. Repeat the above fatigue tests under in-air and PWR-water environment. This is for any representative strain rate for in-air condition (since under 350 ^{o}C i.e., the maximum RCS temperature of a LWR, strain rate effect is negligible). However, since under PWR-water environment, strain rate effect is significant it is suggested to conduct fatigue tests under multiple strain rate to further understand, characterize and codifying (to the DT model) the strain rate effects.

c. Conduct the fatigue tests under temperature control (to mimic the actual reactor loading, refer Figure 3.3 and our earlier publication [5]) rather than following the conventional strain-controlled procedures. Note, under actual reactor condition, strain is the symptom not the actual damage creating variable.

d. Further augment the above temperature-control test methodology by adding mechanical component of loading (associated with component coolant-pressure loading) through additional strain/stress-controlled loading.

e. Improve the PWR-water test methodology (which are primarily done through displacement control since strain cannot be directly measured) to achieve the required strain (at the specimen gauge area) and reducing the effect of cyclic strain hardening (that can result in substantially increased/decreased strain amplitudes and rates compared to the intended strain amplitudes and rates).

References

1. "The Enduring Value of Nuclear Energy Assets." World Nuclear News. 2020. https://www.world-nuclear-news.org/Articles/LTO-essential-to-cost-effective-climate-benefits-o

2. Chopra, O., and Stevens, G. L. 2018. "Effect of LWR Water Environments on the Fatigue Life of Reactor Materials." The U.S. Nuclear Regulatory Commission (NUREG/CR-6909, Revision 1) Final Report. https://www.nrc.gov/docs/ML1631/ML16319A004.pdf

3. "Environmental Fatigue Evaluation Method for Nuclear Power Plants." 2011. Nuclear Energy System Safety Division, Japan Nuclear Energy Safety Organization, JNES-SS-105 (March).https://www.nrc.gov/docs/ML1130/ML113010189.pdf

4. Mohanty, S., and Listwan, J.2020. "A Hybrid AI/ML and Computational Mechanics Based Approach for Time-Series State and Fatigue Life Estimation of Nuclear Reactor Components." Report No. ANL/LWRS-20/01 Argonne National Laboratory. https://doi.org/10.2172/1688432;https://www.osti.gov/biblio/1688432

5. Mohanty, S., and Listwan, J., 2021. "Development of Digital Twin Predictive Model for PWR Components: Updates on Multi Times Series Temperature Prediction Using Recurrent Neural Network, DMW Fatigue Tests, System Level Thermal-Mechanical-Stress Analysis." Report No. ANL/LWRS-21/02. Argonne National Laboratory. https://doi.org/10.2172/1822853; https://www.osti.gov/biblio/1822853

6. Mohanty, S., Soppet, W., Majumdar, S., Natesan, K. 2016. "Thermal-mechanical stress analysis of PWR pressure vessel and nozzles under grid load-following mode: Interim report on the effect of cyclic hardening material properties and pre-existing cracks on stress analysis results." Report No. ANL/LWRS-16/01. Argonne National Laboratory. https://doi.org/10.2172/1249554;https://www.osti.gov/biblio/1249554

7. Mohanty, S., Barua, B., Listwan, J., Majumdar, S., Natesan, K. 2018. Final Report on CFD and Thermal-Mechanical Stress Analysis of PWR Surge Line under Transient Condition Thermal Stratification and an Evolutionary Cyclic Plasticity Based Transformative Fatigue Evaluation Approach without Using S~ N Curve. Report No. ANL/LWRS-17/03 Rev. 1. Argonne National Laboratory. https://doi.org/10.2172/1480513;https://www.osti.gov/biblio/1480513

8. Mohanty, S., Park, J. P., Listwan, J. T. 2019. "A System-Level Framework For Fatigue Life Prediction of PWR Pressurizer-Surge-Line Nozzle under Design-Basis Loading Cycles. A complete tensile test-based material properties database and preliminary results on 3D weld process modeling, thermal-mechanical stress analysis and environmental fatigue testing", Report No. ANL-LWRS-19/01, Argonne National Laboratory. https://doi.org/10.2172/1571258; https://www.osti.gov/biblio/1571258

9. ASME Boiler and Pressure Vessel Code. 2017. "Design by Analysis Sections III and VIII, Division 2." The American Society of Mechanical Engineers. https://www.asme.org

10. Park, J. P., Mohanty, S., Bahn, C. B., Majumdar, S., Natesan, K. 2020. "Weibull and bootstrap-based data-analytics framework for fatigue life prognosis of the pressurized water nuclear reactor component under harsh reactor coolant environment." Journal of Nondestructive Evaluation, Diagnostics and Prognostics of Engineering Systems, 3(1). https://doi.org/10.1115/1.4045162

Nuclear Science and Engineering Division
Argonne National Laboratory
9700 South Cass Avenue, Bldg. 208
Argonne, IL 60439

www.anl.gov

Argonne National Laboratory is a U.S. Department of Energy laboratory managed by UChicago Argonne, LLC